UNIVERSIDAD MICHOACANA DE SAN NICOLÁS DE HIDALGO

FACULTAD DE INGENIERÍA ELÉCTRICA

DIVISIÓN DE ESTUDIOS DE POSGRADO

Periodic and Steady State Assessment of Microgrids with Photovoltaic Generation Sources in Time and Frequency Domain

THESIS

Presented to obtain the Degree of

DOCTOR OF SCIENCE IN ELECTRICAL ENGINEERING

by

M. C. MARCOLINO HUMBERTO DÍAZ ARAUJO

Thesis Advisor

Dr. J. AURELIO MEDINA RIOS

February , 2018

Morelia, Michoacán, Mexico

PERIODIC STEADY STATE ASSESSMENT OF MICROGRIDS WITH PHOTOVOLTAIC GENERATION SOURCES IN TIME AND FREQUENCY DOMAIN

Los Miembros del Jurado de Examen de Grado aprueban la **Tesis de Doctorado en Ciencias de Ingeniería Eléctrica, Opción en Sistemas de Eléctricos de Marcolino Humberto Díaz Araujo.**

Dr. Roberto Tapia Sánchez
Presidente

Dr. J. Aurelio Medina Ríos
Director de Tesis

Dra. Elisa Espinosa Juárez
Vocal

Dr. Antonio Ramos Paz
Vocal

Dr. Manuel Madrigal Martínez
Revisor Externo (Instituto Tecnológico de Morelia)

Dr. Félix Calderón Solorio
Jefe de la División de Estudios de Posgrado
de la Facultad de Ingeniería Eléctrica. UMSNH
(Por reconocimiento de firmas).

UNIVERSIDAD MICHOACANA DE SAN NICOLÁS DE HIDALGO
Febrero de 2018

Dedicated To

My parents: Humberto and Rosa.

For their understanding and unconditional support.

My wife: Rocio.

For loving me the way you do.

My daughter: princess Emi.

For her pure and true love.

My male twins: Marco and Mati.

For becoming my inspiration.

Acknowledgments

First of all, I thank Jesus Christ, the Blessed Virgin Mary, and God almighty for giving me the strength and knowledge to accomplish this dream.

Also, I want to express my sincere thanks:

To Dr. Sc. J. Aurelio Medina Rios for his invaluable support and incessant encouragement.

To CONACYT for the financial support during my master and doctorate studies.

Index

Chapter 1

Chapter 2

Chapter 3

Chapter 4

Chapter 5

List of Symbols and Acronyms

Symbols

Apparent power……S

Boltzmann constant……...k

Capacitance……...C

Control signal……$v_{control}$

Current at MPP……..I_{mpp}

DC component of voltage at PV terminals……V_{pv0}

DC component of current at PV terminals……I_{pv0}

Differentiation matriz……D

Diode ideal constant……..a

Duty ratio……...d

Electron charge……..q

Equivalent Norton current source……..$I_{eq,A}$

Equivalent Norton resistance……....$R_{eq,A}$

Equivalent parallel resistance of the PV module……..R_p

Equivalent series resistance of the PV module……R_s

Frequency……..f

Harmonic current injection vector……I_h

Harmonic voltage vector……V_h

Harmonic equivalent admittance matrix……...Y_h

Inductance……L

Maximum power per module……P_{max}

Modulation index……..m_a

Number of cells connected in series……N_s

Number of modules connected in series……...N_S

Number of modules connected in parallel……N_P

Open circuit voltage……..V_{oc}

Period……T

Period of the fundamental frequency……T_0

PV current……I_{pv}

Reactance……..X

Reactive power……Q

Real power……P

Resistance……R

Rms voltage……..V_{AC}

Short circuit current……...I_{sc}

State transition matrix……...Φ

State vector at the beginning of the base cycle……..x^i

State vector at the end of the base cycle……x^{i+1}

Saturation current……..I_0

Temperature correction factor for current……k_i

Temperature correction factor for voltage……k_v

Terminal current of the PV array……..$I_{pv,A}$

Terminal voltage of the PV array……$V_{pv,A}$

Thermal voltage of the module……V_t

Triangular waveform……v_{tri}

Unit matrix……I

Voltage at MPP……V_{mpp}

Switching period of the BC……T_s

Switching frequency of the BC……F_s

Acronyms

Alternating Current……....AC

Boost Converter……BC

Brute Force……BF

Cubic Spline Interpolation……CSI

Current Injection Method……CIM

Direct Current……...DC

Discrete Fourier Transform……..DFT

Fast Fourier Transform……FFT

Four Order Runge Kutta……...RK4

Frequency Domain……....FD

Harmonic Domain……HD

Maximum Power Point……MPP

Maximum Power Point Tracking……MPPT

Newton Raphson……..NR

Number of Full Time Domain Cycles…….NFT

Numerical Differentiation…….ND

Ordinary Differential Equation…….ODE

Photovoltaic……..PV

Point of Common Coupling……..PCC

Power Factor…….PF

Static VAR Compensator……..SVC

Standard Test Conditions……..STC

Thyristor Controlled Reactor……TCR

Time Domain……TD

Total Harmonic Distortion……...THD

Trapezoidal Rule……..TR

Voltage Source Inverter……VSI

List of Figures

List of Tables

List of Publications

Indexed Conference Papers by ISI Thompson, published papers:

1. **Periodic Steady State Solution of Power Networks using the Current Injection Method and Parallel Processing based on GPUs**, M. H. Díaz-Araujo, A. Medina-Rios, E. Magaña-Lemus, A. Ramos-Paz, The 2016 World Congress in Computer Science, Computer Engineering, and Applied Computing, Las Vegas, Nevada, USA, July 25-28, 2016.
2. **Periodic Steady State Solution of Power Networks using the Numerical Differentiation Method and Spline Interpolation**, M. H. Díaz-Araujo, A. Medina-Rios, The 2017 IEEE PES General Meeting, Chicago, Illinois, USA, July 16-20, 2017.
3. **Periodic Steady State of Power Networks using Limit Cycle Extrapolation, Spline Interpolation and parallel processing based on GPUs**, M. H. Díaz-Araujo, A. Medina-Rios, E. Magaña-Lemus, The 2017 Computational Science and Computational Intelligence, Las Vegas, Nevada, USA, December 14-16, 2017.

Indexed by Journal Citation Reports (JCR), under review:

1. **Dynamic and Steady State Assessment of Electrical Networks with Photovoltaic Generation Sources using Limit Cycle Extrapolation and Cubic Splines**, M. H. Díaz-Araujo, A. Medina-Rios, A. Ramírez-Vázquez, R. Cisneros-Magaña, Renewable Energy, Elsevier.

Abstract

This thesis presents two fast and accurate methodologies for the assessment of the dynamic and periodic steady state operation of microgrids with photovoltaic energy sources in time and harmonic domain. The topology of the entire electrical system involves a photovoltaic array connected to a boost converter, followed by an inverter which is coupled to the electrical network via a passive filter.

The time domain methodology uses the trapezoidal rule technique to integrate the set of first-order differential algebraic equations, generated by the entire electrical system. Then, the numerical differentiation method is used to significantly speed-up the process of convergence of the state variables to the limit cycle. After that, the cubic spline interpolation algorithm is used to reconstruct the steady state waveform obtained from the numerical differentiation method to the fewest number of possible time steps. This curve fitting algorithm is used only once the steady state is obtained. The efficiency of the solution is further enhanced with the application of parallel processing based on Graphic Processing Units.

The harmonic domain methodology is based on the Fourier series to express voltages/currents as vectors and admittances/impedances as matrices, this allows to include frequencies multiples of the fundamental frequency, i.e., harmonics. The PV array is represented as a Thevenin equivalent in the Harmonic Domain. The boost converter and the inverter are represented in the harmonic domain via switching function matrices. This allows to obtain the steady state of the entire electrical system via simple matrix/vector operations.

The results are successfully validated through direct comparison against those obtained with the PSCAD/EMTDC simulator, widely accepted by the power industry. The main applications of the proposed methodologies are in the areas of power quality and of distributed generation.

In addition, this thesis details an efficient algorithm for the simulation of the steady state response of power networks under non-sinusoidal conditions. The algorithm uses the current injection method, LU decomposition, and parallel processing based on graphic processing units. It is shown that the implementation on a graphic processing unit platform becomes an

efficient computational resource to find the steady state solution since floating-point operations and repetitive calculations increase in proportion to the size of the network.

Resumen

Esta tesis presenta dos metodologías rápidas y precisas para la evaluación de la operación dinámica y de estado estable de micro redes con fuentes de energía fotovoltaica en el dominio armónico y del tiempo. La topología del sistema eléctrico completo consta de un arreglo fotovoltaico conectado a un convertidor Boost, seguido de un inversor el cual está conectado a la red eléctrica mediante un filtro pasivo.

La metodología en el dominio del tiempo utiliza la técnica de la regla trapezoidal para integrar el conjunto de ecuaciones diferenciales algebraicas, generadas por el sistema eléctrico completo. Entonces, el método de diferenciación numérica se utiliza para acelerar significativamente el proceso de convergencia de las variables hacia el ciclo límite. Después de esto, el algoritmo de interpolación segmentaria cubica se usa para reconstruir la forma de onda de estado estable obtenida por el método de diferenciación numérica con el menor número posibles de muestras por periodo. El algoritmo de ajuste de curvas se utiliza una vez que se ha obtenido el estado estable. La eficiencia de la solución es aun mejorado con la aplicación de procesamiento en paralelo basado unidades de procesamiento gráfico.

La metodología en el dominio armónico está basada en el análisis de Fourier para expresar los voltajes y/o corrientes como vectores y las admitancias y/o impedancias como matrices, lo cual permite incluir frecuencias múltiplos de la fundamental, esto es, armónicos. El arreglo fotovoltaico se presenta como un equivalente de Thevenin en el dominio armónico. El convertidor boost y el inversor son representados en el dominio armónico por medio de matrices con funciones de conmutación. Esto permite obtener el estado estable del sistema eléctrico completo por medio de operaciones con matrices y/o vectores.

Los resultados son exitosamente validados a través de la comparación directa con el simulador PSCAD/EMTDC, ampliamente reconocido por la industria. Las aplicaciones principales de las metodologías propuestas se encuentran el área de la calidad de la energía y en sistemas de generación distribuida.

Además, esta tesis describe un algoritmo eficiente para la simulación de la respuesta en estado estable de redes eléctricas bajo condiciones no senoidales. El algoritmo utiliza el método de inyección de corrientes, la factorización LU y procesamiento en paralelo basado

en unidades de procesamiento gráfico. Se ha probado que la implementación sobre una plataforma basada en unidades de procesamiento gráfico se convierte en un recurso eficiente computacional para encontrar la solución en estado estable, ya que las operaciones con punto flotante y los cálculos repetitivos se incrementan en proporción al tamaño de la red.

Palabras clave: Dominio-Tiempo, Dominio-Armónico, Sistema Fotovoltaico, Procesamiento en Paralelo y Estado Estable.

Chapter 1

Introduction

1.1 Introduction

Last decade, the use of renewable energies for producing electrical power has increase exponentially. Several countries around the world are interested in natural and clean sources of energy as an alternative for protecting the natural environment. Among the renewable energies available for producing electrical power, solar energy is one of the most promising.

Sunlight can be transformed to electricity through a photovoltaic (PV) device. A PV device is basically a semiconductor diode whose p-n junction is exposed to light [Moller 1993]. The incidence of light on the semiconductor generates charge carriers that originate an electric current if the cell is short-circuited. To date, there is a wide variety of semiconductors using different manufacturing processes. The monocrystalline and polycrystalline silicon semiconductors are the only found at commercial scale [Patel 2006], [Messenger and Ventre 2010]. For the purposes of this thesis, these two materials have similar behavior and are not studied in detail.

The basic device of a PV system is the PV cell. Due to the low voltage produced by a PV cell, a set of PV cells may be grouped to form panels or modules [Masters 2004]. Most PV panels available on the market are normally constituted by 36 or 72 PV cells connected in series/parallel. The power output ratings of PV panels ranging from 300 to 500 W.

When the desired power of the PV panel is insufficient, a combination of PV panels connected in series/parallel is implemented. The combination is called PV array.

The connection of a PV array with the microgrid is normally achieved by using a DC capacitor link, a DC/DC converter, a DC/AC converter, and a filter. This PV generation system produce harmonics that interact with the microgrid adversely affecting power quality.

The dynamic and periodic steady state condition of these PV generation systems is important for the planning, design and operation of electrical networks and power systems where they are connected.

Reported technical problems and limitations of PV generation are its variability, intermittency and adverse power quality effects, such as harmonic distortion, voltage and frequency variations, among others. In particular, this thesis centers on the analysis of the harmonic distortion produced by PV generation systems in microgrids. These problems can be analyzed with the proposed time and frequency domain methodologies. Both can be applied to take adequate control decisions, i.e., to regulate the power generation and the energy conversion process or to enhance the electrical network or microgrid stability, among other issues.

1.2 State of the Art

Aside from the depleting fossil fuel reserve, the concern for global warming has become an impetus across the world to integrate PV generation systems in the conventional power systems. Usually, PV generation systems of single digit MW capacities have been connected to the power system, primarily, at subtransmission voltage levels. However, such PV generation systems are expected to be increasingly connected to distribution networks where loads and/or other local generators are also present. This calls for better understanding of large-scale PV systems employed as distributed energy sources, in terms of control, dynamic characteristics, and performance, through development of suitable simulation models [Willis and Scott 2000].

In Germany, Australia, and other developed countries, large-scale PV systems [Martin Bucher 2016], [Victorian Project 2017] are either already embedded or expected to be integrated in the conventional high voltage grid in the next few years. Nevertheless, any information on their operating strategies is yet to be made available. However, significant work [Tan *et al*. 2004], [Lee and Wang 2008] has been done on small-scale PV generation systems only and operating with or without a parallel alternate source, e.g., capacitor bank, battery, fuel cell, diesel generator, or wind turbine.

The system was either an isolated one [Sokolov and Shmilovitz 2008], [Chen *et al*. 2010] or interfaced with the utility [Tan *et al*. 2004], [Jain and Agarwal 2008] at the low voltage side (230 V).

On the other hand, the steady state response of power networks with interconnected PV generation systems is now of primary interest to an engineer. This is because certain aspects of system performance are easier to characterize and verify in steady state. Examples of quantities that are best measured when the power system is in steady state include harmonic distortion, power, frequency, etc.

The periodic steady state solution of a power network can be obtained in three main frameworks, i.e., time domain (TD), frequency domain (FD) and hybrid frequency-time domain, respectively. A concise review is given in [Medina *et al*. 2013] regarding the main advantages, drawbacks, formulation and convergence characteristics related to the different methods belonging to the frames of reference above indicated.

In the TD framework, the work presented in [Tan *et al*. 2004] describes a model of PV generation suitable for studying its interactions with the power system. Four years later, [Lee and Wang 2008] applied a TD technique to obtain the dynamic response of a hybrid renewable generation system connected to isolated loads, and [Jain and Agarwal 2008] developed a model for distributed generation applications fed by nonconventional energy sources. In those works, the focus was basically on the analysis of stability. Needless to say, the findings from analyses or tests using such small-scale models at the end user level cannot be applied for evaluating the operational impacts of large-scale PV systems interfaced with the high voltage buses in a grid.

Another way to compute the periodic steady state response of a PV generation system in the specialized literature in TD is via simulation packages [Perera *et al*. 2012], [Sood and Balla 2009], for instance PSCAD/EMTDC [PSCAD 2005], PSIM [PSIM 2016] or EMPT-RV [EMPT-RV 2012]. Harmonic analysis is then performed as a post-processing procedure.

In the harmonic domain (HD) framework several models of power systems components have been developed, for example, synchronous machine [Xu *et al*. 1991], [Medina *et al*. 1994], the power transformer [Medina and Arrillaga 1992], [Semlyen *et al*. 1997], arc furnaces [Acha *et al*. 1990], fluorescent lamps [Chang 2003], Thyristor Commutated Reactors (TCRs) [Acha *et al*. 1996], the power converters [Smith *et al*. 1995], [Bathrurst *et al*. 2001], HVDC systems [Bathrurst *et al*. 2000], adjustable speed drives [Xu *et al*. 2000], static var systems [Xu *et al.* 1999], and the unified power flow controller (UPFC) [Collins *et al*. 2006].

However, single-phase grid-connected PV generation systems have not been fully modelled in the HD. Some electronic components used in grid-connected PV generation systems have been modelled in HD separately, for instance the voltage source inverter (VSI) [Acha and Madrigal 2001], but with distinct applications.

1.3 Motivation Behind the Present Research

Generally, TD methods have been used to simulate single-phase grid-connected PV generation systems where a post-processing stage is needed for harmonic visualization. Furthermore, TD methods may require integration over considerable periods of time. It has been suggested only for cases where the periodic steady state response can be obtained in a few cycles [Dommel *et al*. 1986], such as sufficiently damped systems. Otherwise, achieving steady state requires long simulation times and large computational resources.

Fortunately, there are techniques to speed-up the convergence process. The extrapolation to the limit cycle and Poincaré map techniques have been applied to quickly obtain the periodic steady state of electrical systems. They were first introduced in [Semlyen and Medina, 1995]. A follow-up research in this field is reported in [Segundo and Medina 2008], [Segundo 2010]. The Numerical Differentiation (ND) method is one of the extrapolation to the limit cycle techniques introduced in [Semlyen and Medina 1995]. In the present research, the ND method is used to speed-up the periodic steady state solution of the microgrid with interconnected PV generation.

The cubic splines interpolation (CSI) is an algorithm that has been applied to accurately estimate a new point between known data with smaller error that the obtained with square or linear interpolation. The application of the CSI method is proposed to adjust the number of times steps per cycle needed during the TD solution.

HD techniques constitute alternative methods for the modelling and simulation of electrical systems with emphasis on the analysis of the quality of power. HD simulations provide the steady state solution of a system in a direct manner and power quality indices are readily available.

1.4 Aims

1.4.1 Main Aim

- Main aim: To implement a fast and accurate time and frequency domain methodology for the assessment of the dynamic and periodic steady state operation of microgrids with photovoltaic energy sources.

1.4.2 Particular Aims

- To incorporate in the TD solution process, efficient numerical techniques, such as Newton methods, extrapolation to the limit cycle, and cubic splines interpolation.
- To assure the Maximum Power Point (MPP) operation of the PV array in the HD method. Besides, the proposed model should be able to account for any number of harmonics.
- To develop the digital tools for the assessment of the dynamic and periodic steady state operation of microgrids with PV energy sources in Time and Harmonic Domains, respectively.
- To develop an efficient algorithm for the simulation of the steady state response of power networks under non-sinusoidal conditions using parallel processing techniques based on graphic processing units (GPUs)

1.5 Contributions

The main contributions of this work can be summarized as follows:

- A fast and accurate time and frequency domain methodology for the assessment of the dynamic and periodic steady state operation of microgrids with photovoltaic energy sources. The TD solution process incorporates efficient numerical techniques and the HD model is capable to account for any number of harmonics.
- A time and frequency domain simulator with efficient and accurate mathematical and numerical tools such as Newton Raphson (NR), Trapezoidal Rule (TR) and Parallel Processing based on GPUs.
- A fast and efficient algorithm for harmonic propagation studies using advanced computational and mathematical tools.

1.6 Thesis Outline

Chapter 1 presents a review of the state of the art associated with the methods that have been used to simulate single-phase grid-connected PV generation systems in time and frequency domains. After this review of the state of the art, aims, motivation and contributions to be achieved are established. Finally, the description of chapters are given.

Chapter 2 presents the numerical and computational tools used to develop this thesis, such us, NR, TR, DFT, FFT and Parallel Processing based on GPUs.

Chapter 3 deals with the description and modeling of the single-phase grid-connected PV generation system in TD, a review of the ND method based on the Poincaré map and extrapolation to the limit cycle concepts, and an explanation of the CSI technique. Also, a case study for harmonic propagation in TD using parallel processing based on multi-CPUS and multi-GPUs is shown.

Chapter 4 describes a HD technique for the modelling and simulation of single-phase grid-connected PV generation system. The fundamentals of HD and the representations of basic electrical elements in HD are presented. Also, some power quality indices for

nonsinusoidal conditions are given. In addition, a case study for harmonic propagation in FD is presented.

Chapter 6 presents the general conclusions drawn from this research, addressing and suggesting ideas for further research to be done in the same field of knowledge.

Chapter 2

Numerical and Computational Techniques

2.1 Introduction

Nowadays, power systems analysis methodologies require solving complex and highly non-linear problems, which requires the use of a large amount of computational resources. Therefore, power system simulations must incorporate advanced numerical and computational techniques for planning, operation, control, and analysis. In other words, a simulation technique must be fast, computationally efficient, robust, secure, and reliable. At the same time, it is necessary to make models as efficient as possible to minimize computation times and to capture realistic effects. This chapter gives a concise description of the numerical mathematical and computational tools incorporated in this research work with the aim of making the solution process involved for each case robust, reliable and efficient. These are the following:

- The Newton Raphson Method.
- Trapezoidal Rule.
- Parallel Processing Techniques Based on GPUs.
- Discrete Fourier Transform
- Fast Fourier Transform

2.2 Newton Raphson Method

Equation (3.1) is an algebraic and transcendental equation, i.e., is a nonlinear equation. In order to find the solution, it is necessary to use a numerical method. Perhaps the most widely used to find the solution of a nonlinear equation is the NR Method.

The derivation of the NR method is as follows: a current guess is x and this is incorrect by an amount of h, so that $x+h$ is the exact value of the sought root. It now remains for us to determine h or at least find an approximation to it.

The Taylor expansion for the function $f(x)$ at the point $x + h$ is given by [Otto and Denier 2005]:

$$f(x + h) = f(x) + hf'(x) + O(h^2) \tag{2.1}$$

This can be interpreted as follows: the value of the function at $x+h$ is equal to the value of the function at x plus the gradient times the distance between the points. This can be considered to include further terms; at the moment we are fitting a straight line.

In this expression we have used the term $O(h^2)$: loosely this means something the same size as h^2 and also the prime means differentiated with respect to the argument of the function. We now note that $x+h$ is supposedly the actual root so $f(x+h)=0$. Discarding the higher-order terms from (2.1) we find that,

$$h \approx -\frac{f(x)}{f'(x)} \tag{2.2}$$

This presumes that the actual root is close, and consequently we can discard the terms proportional to h^2, since these should be smaller than those proportional to h.

This allows us to construct the iterative recursive equation,

$$x_{n+1} = x_n - \frac{f(x_n)}{f'(x_n)}, \quad n = 0,1,2, \ldots \tag{2.3}$$

2.3 The Trapezoidal Rule

The Newton-Cotes formulas are the most common numerical integration schemes. They are based on the strategy of replacing a complicated function or tabulated data with an approximation function that is easy to integrate [Chapra and Canale 2010]:

$$I = \int_a^b f(x)dx \cong \int_a^b f_n(x)dx \tag{2.4}$$

where $f_n(x)=a$ is a polynomial of the form

$$f_n(x) = a_0 + a_1 x + \cdots + a_{n-1} x^{n-1} + a_n x^n$$

where n is the order of the polynomial.

The TR is the first of the Newton-Cotes closed integration formulas. It correspond to the case where the polynomial in (2.4) is first-order:

$$I = \int_a^b f(x)dx \cong \int_a^b f_1(x)dx$$

where

$$f_1(x) = a_0 + a_1 x = f(a) + \frac{f(b)-f(a)}{b-a}(x-a) \tag{2.5}$$

The area under this straight line is an estimate of the integral of $f(x)$ between the limits a and b:

$$I = \int_a^b \left[f(a) + \frac{f(b)-f(a)}{b-a}(x-a) \right] dx$$

The result of the integration is

$$I = (b-a)\frac{f(a)+f(b)}{2} \tag{2.6}$$

which is called the TR and is an example of an implicit method.

2.4 Parallel Processing Techniques Based on GPU

2.4.1 An Overview on GPUs

A graphic processing unit (GPU) is a co-processor dedicated to graphics processing and floating point operations. A GPU helps to offload tasks from CPU. Generally the GPU is connected to the CPU and is completely separate from the motherboard. The random access memory (RAM) is connected through the accelerated graphics port (AGP) or the peripheral component interconnect express (PCI-Express) bus.

Some GPUs are integrated into the northbridge on the motherboard and use the main memory as a digital storage area, but these GPUs are slower and have poorer performance [Cook 2013].

A GPU has parallel processing architecture, which allows it to perform multiple calculations on sets of data at the same time. The GPU, first invented by Nvidia, is the most powerful parallel processor to date [Sanders and Kandrot 2010].

2.4.2 Fermi Architecture

Nvidia is one of the leading manufactures of GPUs. Architecture Fermi and Kepler are the most widely used for parallel processing. The GPU used in this research is the Tesla C2075 with Fermi architecture, discussed next [Nvidia Fermi 2011].

The Tesla C2075 [Nvidia Fermi 2011] is implemented with 3.0 billion transistors, features up to 512 CUDA cores. A CUDA core executes a floating point or integer instruction per clock for a thread. The 512 CUDA cores are organized in 16 streaming multiprocessors (SM) of 32 cores each. The GPU has six 64-bit memory partitions, for a 384-bit memory interface, supporting up to a total of 6 GB of GDDR5 DRAM memory. The Giga Thread global scheduler distributes thread blocks to SM thread schedulers.

Fig. 2.1 shows the elements of a SM and a CUDA core. A brief explanation of the components of the Fermi SM is given below:

- **Load/Store Units**. Each SM features 32 CUDA processors and has 16 load/store units, allowing source and destination addresses to be calculated for sixteen threads per clock. Supporting units load and store the data at each address to cache or DRAM.
- **Four Special Fuction Units**. A special function unit (SFU) execute transcendental instructions such as sine, cosine, reciprocal, and square root. The SFU pipeline is decoupled from the dispatch unit, allowing the dispatch unit to issue other execution units while the SFU is occupied.

- **Dual Warp Scheduler**. The SM schedules threads in groups of 32 parallel threads called warps. Each SM features two warp schedulers and two instruction dispatch units, allowing two warps to be issued and executed concurrently. Fermi's dual warp scheduler selects two warps, and issues one instruction from each warp to a group of sixteen cores, sixteen load/store units, or four SFUs.
- **Shared Memory and L1 Cache**. Shared memory enables threads within the same thread block to cooperate, facilitates extensive reuse of on-chip data, and greatly reduces off-chip traffic.

Each CUDA processor has a fully pipelined integer arithmetic logic unit (ALU) and floating point unit (FPU).

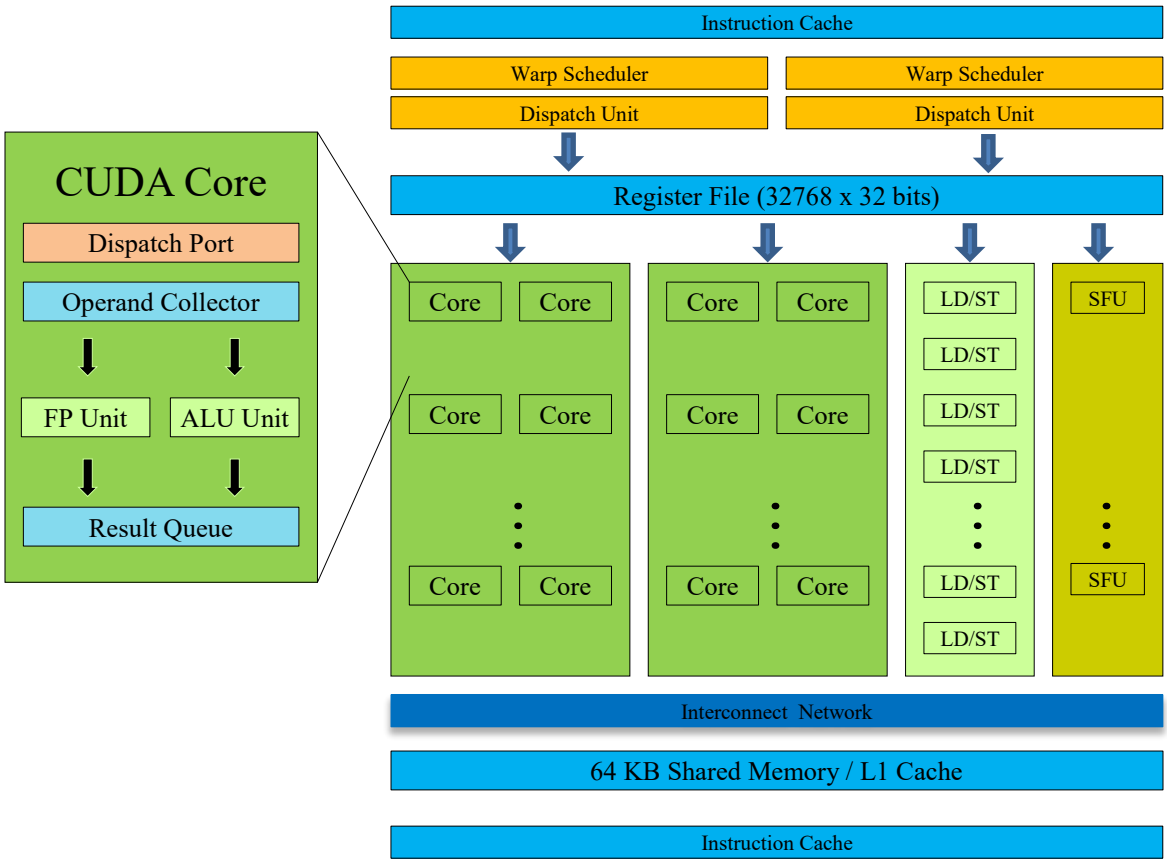

Fig. 2.1 SM and core processor scheme.

2.4.3 Kepler Architecture

Kepler Architecture is the successor to the Fermi Architecture. Kepler introduces two key changes that greatly improve the GPU´s efficiency. First, a redesigned SM, the most important building block of the GPU, for optimal performance per watt. Kepler´s SM has twice the performance per watt compared to the Fermi´s SM. Second, a feature called GPU Boost that dynamically increases clock speed to improve performance within the card´s power budged [Nvidia Kepler 2012].

The most important thing to understand about GPU Boost is that it works through real time hardware monitoring as opposed to application based profiles. As an algorithm, it attempts to find what is the appropriate GPU frequency and voltage for a give moment in time. It does this by reading a huge swathe of data such as GPU temperature, hardware utilization, and power consumption. Depending on these conditions, it will raise the clock and voltage accordingly to extract maximum performance within the available power envelop. Because all this is done via real-time hardware monitoring, GPU Boost requires no application profiles.

2.4.4 CUDA

CUDA is the hardware and software architecture that enables Nvidia GPUs to execute programs written with C, C++, Fortran, OpenCL, DirectCompute, and other languages [Nvidia CUDA 2015]. A CUDA program calls parallel kernels. A kernel executes in parallel across a set of parallel threds. The programmer or compiler organizes these threads in thread blocks and grids of threads blocks. The GPU instantiates a kernel program on a grid of parallel thread blocks. Each thread within a thread block executes an instance of the kernel, and has a thread ID within its thread block, program counter, registers, per-thread private memory, inputs, and output results.

A thread block is a set of concurrently executing threads that can cooperate among themselves through barrier synchronization and shared memory. A thread block has a block ID within its grid.

A grid is an array of thread blocks that execute the same kernel, read inputs from global memory, write results to global memory, and synchronize between dependent kernel calls. In the CUDA parallel programing model, each thread has a per-thread private memory space used for register spills, function calls, and C automatic array variables. Each thread block has a per-block shared memory space used for inter-thread communication, data sharing, and result sharing in parallel algorithms. Grids of thread blocks share results in global memory space after kernel-wide global synchronization.

A CUDA program has two parts: the serial part and the parallel part. In the serial part, no parallelism exists and the instructions are executed in the CPU. In the parallel part, which involves massive data parallelism, instructions are executed in the GPU. A high level view of the CUDA programming model is illustrated in Fig. 2.2.

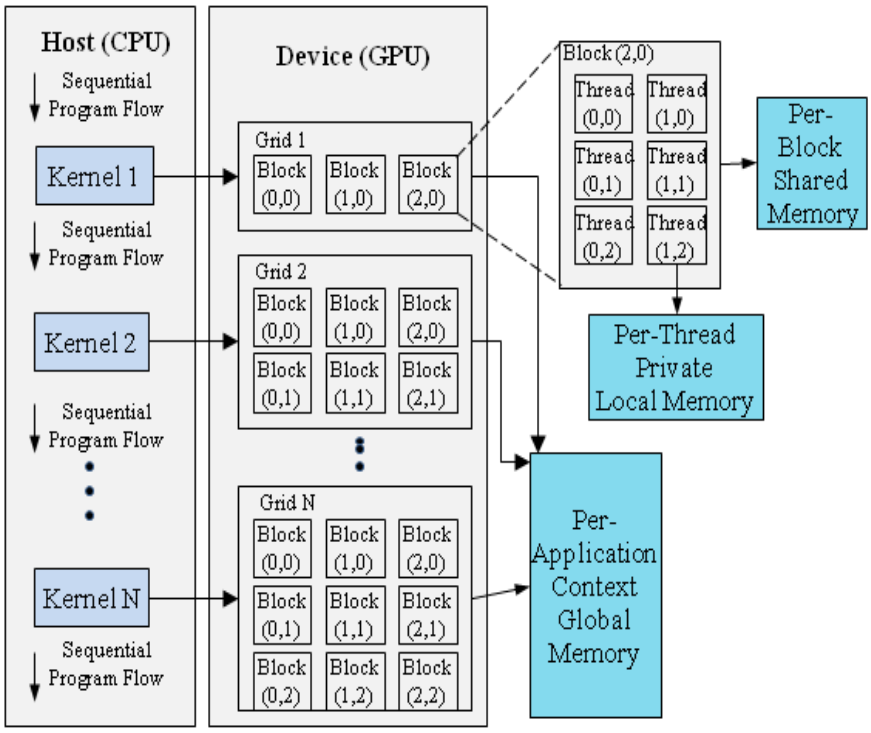

Fig. 2.2 Schematic of execution of a Nvidia´s CUDA programming model.

2.4.5 OpenMP

Open MP is an application programming interface (API) for parallel programming on multiprocessors. It consists of a set of compiler directives and a library of support functions. OpenMP works in conjunction with standard C, or C++ [Quinn 2004].

The OpenMP API uses the *fork-join* model of parallel execution. Under this approach, the program starts as a single thread of execution, just like a sequential program. The thread that executes this code is referred to as the initial thread. Whenever an OpenMP parallel construct is encountered by a thread while it is executing the program, it creates a team of threads (this is the *fork*), becomes the master of the team, and collaborates with the other members of the team to execute the code dynamically enclosed by the construct. At the end of the construct, only the original thread, or master of the team, continues; all others terminate (this is the *join*). Each portion of code enclosed by a parallel construct is called a parallel region [Chapman *et al.* 2008].

The OpenMP API comprises a set of compiler directives, runtime library routines, and environment variables to specify shared-memory parallelism in C or C++ programs. An OpenMP directive is a specially formatted comment or pragma that generally applies to the executable code immediately following it in the program. A directive or OpenMP routine generally affects only those threads that encounter it.

A team of threads is created to execute the code in a parallel region of an OpenMP program. To accomplish this, the programmer simply specifies the parallel region by inserting a parallel directive immediately before the code that is to be executed in parallel to mark its start. Additional information can be supplied along with the parallel directive. This is mostly used to enable threads to have private copies of some data for the duration of the parallel region and to initialize that data. At the end of a parallel region is an implicit barrier synchronization: this means that no thread can progress until all other threads in the team have reached that point in the program.

If the programmer does not specify how the work in a parallel region is to be shared among the executing threads, they will each redundantly execute all of the code.

The OpenMP work-sharing directives are provided for the programmer to state how the computation in a structured block of code is to be distributed among the threads.

OpenMP is based on the shared-memory model; hence, by default, data is shared among the threads and is visible to all of them. Sometimes, however, one needs variables that have thread-specific values. When each thread has its own copy of a variable, so that it may potentially have a different value for each of them, we say that the variable is *private*. For example, when a team of threads executes a parallel loop, each thread needs its own value of the iteration variable. This case is so important that the compiler enforces it; in other cases the programmer must determine which variables are shared and which are private. Data can be declared to be shared or private with respect to a parallel region or work-sharing construct.

Synchronizing, or coordinating the actions of, threads is sometimes necessary in order to ensure the proper ordering of their accesses to shared data and to prevent data corruption. By default, OpenMP gets threads to wait at the end of a work-sharing construct or parallel region until all threads in the team executing it have finished their portion of the work. Only then can they proceed. This is known as a barrier.

2.5 Discrete Fourier Transform

In practice, data is often available in the form of a sampled time function, represented by a time series of amplitudes, separated by fixed time intervals of limited duration. When dealing with such data, a modification of the Fourier transform, the discrete Fourier transform (DFT), is used [Proakis and Manolakis 1996], [Acha and Madrigal 2001]. The DFT is computed with

$$X[n] = \sum_{k=0}^{N-1} x[k] e^{-j2\pi kn/N} \tag{2.7}$$

where *N* represents the number of samples. The inverse discrete Fourier Transform (IDFT) is

$$x[k] = \frac{1}{N} \sum_{n=0}^{N-1} X[n] e^{j2\pi kn/N} \tag{2.8}$$

Also, the DFT and IDFT can be seen as a linear transformation represented by:

$$X = Wx \tag{2.9}$$

$$x = UX \tag{2.10}$$

In (2.9) and (2.10), the matrices W and U are formed by the typical terms $e^{-j2\pi kn/N}$ and $e^{j2\pi kn/N}$ from (2.7) and (2.8), respectively.

2.6 Fast Fourier Transform

The phasor terms within the transformation matrices in (2.9) and (2.10) are repeated according to the value of *N*. The FFT algorithm takes advantage of this repetition and applies an efficient solution scheme that achieves the transformation with a reduced number of operations, thus considerably saving computational time [Proakis and Manolakis 1996], [Acha and Madrigal 2001].

The application of the DFT (or FFT) to a TD sampled signal results in a vector with its frequency components arranged as:

$$X = \begin{bmatrix} X_0 \\ X_1 \\ X_2 \\ \vdots \\ X_{N/2} \\ X_{N/2} \\ \vdots \\ X_2^* \\ X_1^* \end{bmatrix} \tag{2.11}$$

In (4.18), the subscript of each element denotes the number of the frequency component, and "*" denotes the complex conjugate. The frequency spacing (Δf) between components is related to the period of observation of the TD signal (T_{max}), as follows:

$$\Delta f = 1/T_{max} \tag{2.12}$$

It should be noted that if we apply the FFT to a TD signal with $T_{max} = T_0$, Δf results equal to f_0, such that the frequency components in (2.11) are harmonics of f_0. This consideration will be used through the remaining of this thesis.

2.7 Conclusions

This chapter has presented the advanced mathematical and computational tools used for the development of this research work. A concise basic theory of the NR Method, TR approximation, parallel processing based on GPUs, DFT, and FFT has been given.

Chapter 3

PV Systems Modelling in Time Domain

3.1 Introduction

Renewable PV generation systems represent an attractive and viable alternative of electrical energy supply to decrease the environmental contamination and the global warming due to the consumption of fossil fuels. The PV installations have been steadily growing over the last decades. At present, a considerable number of PV generation plants are connected to power systems or to isolated electrical networks [Eltawil and Zhao 2010].

The dynamic performance of these PV generation systems is important for the planning, design and operation of electrical networks and power systems where they are connected [Kouro *et al*. 2015]. This chapter mainly focuses in a TD framework for the representation of these interconnected PV generation systems working under dynamic and periodic steady state conditions [Kim *et al.* 2009]. The proposed methodology is based on a set of first-order differential algebraic equations (DAEs) to represent the entire electrical system. The extrapolation to the limit cycle and Poincaré map approach [Parker and Chua 1989] is used to quickly obtain the periodic steady state. The CSI is an algorithm to accurately estimate a new point between known data with smaller error that the obtained with square or linear interpolation [Chapra and Canale 2010], [Burden *et al.* 2011]. The application of the CSI is proposed to adjust the number of time steps per cycle needed during the TD solution. The CSI technique accurately obtains new solution points, adjusted with a smaller error.

3.2 System Description and Modelling

Fig. 3.1 shows the configuration of a single-phase grid-connected PV generation system. It contains a PV array, a capacitor link, a DC/DC converter, a DC/AC converter, a filter, and a utility grid [Morales 2014].

The capacitor link is connected at the output of the PV array for decoupling AC-system dynamics from the PV array. The DC/DC converter is used to maintain an adequate voltage level and for maximum power point tracking (MPPT) of the PV generation system. The DC/AC converter is used to obtain AC power. Finally, the filter is used to mitigate the total harmonic distortion (THD) at the point of common coupling (PCC).

3.2.1 PV Array Model

A PV cell is the basic unit of a PV array. Typically, a single PV cell generates an electrical power of about 1 to 3 W. To increase the power, several PV cells are connected in the appropriate series-parallel combination to form larger capacity units, called PV modules. Fig. 3.2 shows the equivalent circuit of a practical PV module. The equation from the theory of semiconductors [Rauschenbach 1980], [Kalogirou 2013] that mathematically describes the characteristic of a PV module is

$$I = I_{pv} - I_0 \left[exp\left(\frac{V+R_S I}{V_T a}\right) - 1 \right] - \frac{V+R_S I}{R_p} \tag{3.1}$$

where I_{pv} and I_0 are the PV and saturation currents of the PV module, respectively. $V_T = N_s kT/q$ is the thermal voltage of the module with N_s cells connected in series, q is the electron charge ($1.60217646 \times 10^{-19}$ C), k is the Boltzmann constant ($1.3806503 \times 10^{-23}$ J/K), and T is the temperature on the *p-n* junction (in Kelvin degrees). In (2.1), a is the diode ideal constant, R_s is the equivalent series resistance of the PV module (Ω), and R_p is the equivalent parallel resistance (Ω).

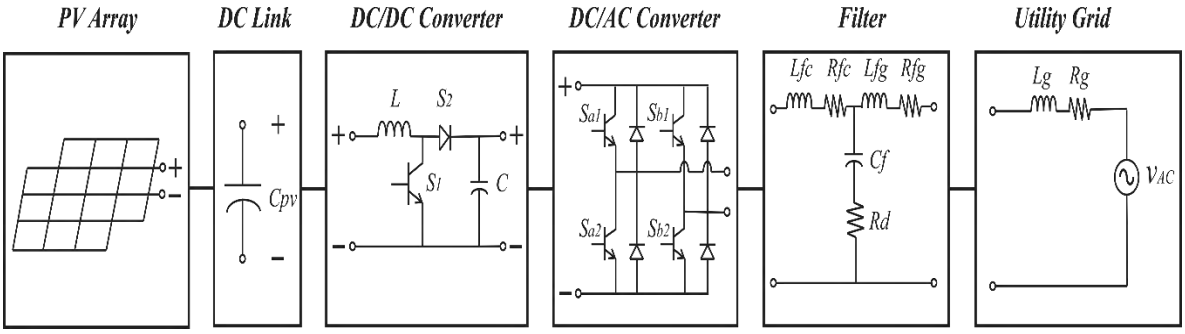

Fig. 3.1 Single-phase grid-connected PV generation system.

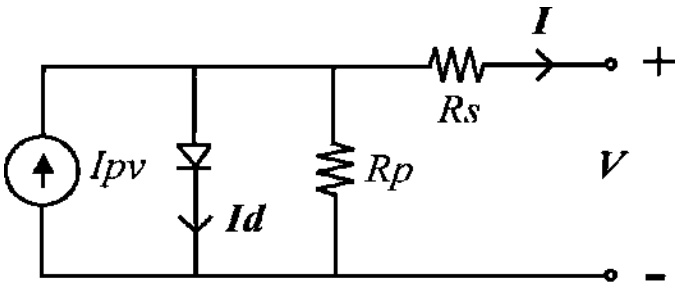

Fig. 3.2 Single-diode model of the theoretical equivalent circuit of a PV module.

From (3.1) the V-I curve of Fig. 3.3(a) is obtained, where three particular points are highlighted, i. e., short circuit (0,I_{sc}), MPP (V_{mpp}, I_{mpp}), and open circuit (V_{oc}, 0) [Villalva *et al.* 2009]. The V-P curve of Fig. 3.3(b) also dictates the performance of a PV module.

A PV array consists of N_P parallel and/or N_S series connected modules. To include a PV array model in the PV generation system, a PV Thevenin equivalent is obtained in this thesis based on the calculation of the R_p and R_s parameters of the model of Fig. 3.2. Basically, this is achieved by solving the nonlinear relation (3.1), considering the PV array working at MPP.

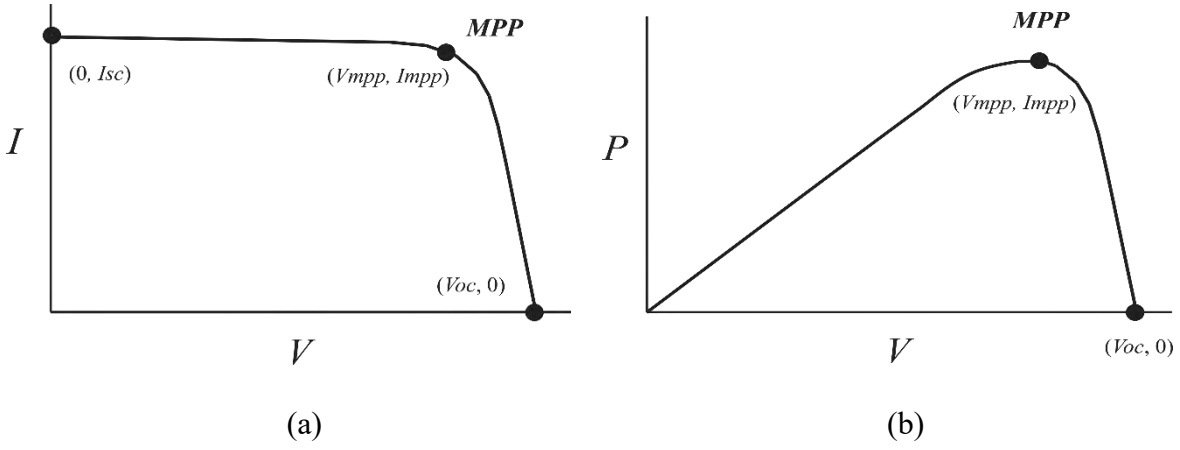

Fig. 3.3 (a) Characteristic I-V of a PV module, (b) characteristic V-P of a PV module.

The calculation of the PV Thevenin equivalent follows the next steps:

Step 1. When a PV array is assembled, V_{oc} and I_{sc} are proportional to the number of series and parallel connected modules, respectively. The total PV array characteristics are calculated with:

$$V_{OC} = N_S V_{oc} \tag{3.2a}$$

$$V_{MPP} = N_S V_{mpp} \tag{3.2b}$$

$$I_{SC} = N_P I_{sc} \tag{3.2c}$$

$$I_{MPP} = N_P I_{mpp} \tag{3.2d}$$

Step 2. We assume that I_{PV} of the adopted model equals the maximum possible generated current (I_{SC}). This permits to calculate I_0 by using:

$$I_0 = \frac{I_{SC}}{exp^{\frac{V_{OC}}{aV_T}} - 1} \tag{3.3}$$

Step 3. Considering that the PV array works at MPP, we evaluate (3.1) at the MPP, obtaining:

$$I_{MPP} = I_{PV} - I_0 \left[exp\left(\frac{V_{MPP} + I_{MPP} R_S}{V_T a}\right) - 1 \right] - \frac{V_{MPP} + I_{MPP} R_S}{R_P} \tag{3.4}$$

Also, from Fig. 3.3(b) it can be notice that the derivative of the power with respect to the voltage is zero at the MPP. This condition is described by:

$$\frac{I_{MPP} R_S - V_{MPP}}{V_T a} I_0 exp^{\frac{V_{MPP} + I_{MPP} R_S}{V_T a}} + I_{MPP}\left(\frac{R_S}{R_P} + 1\right) - \frac{V_{MPP}}{R_S} = 0 \tag{3.5}$$

Thus, (3.4) and (3.5) are solved simultaneously in order to obtain R_S and R_P, for instance by using the NR.

Step 4. Once R_S and R_P are known from the solution of (3.4) and (3.5), and following the Thevenin theorem, the equivalent voltage source is obtained with:

$$V_{th} = R_P \left[I_{PV} - I_0 \left(exp^{\frac{V_{MPP} + I_{MPP} R_S}{V_T a}} - 1 \right) \right] \tag{3.6}$$

and the equivalent resistance is given by:

$$R_{th} = R_P + R_S \tag{3.7}$$

The resultant Thevenin equivalent given by (3.6) and (3.7) is finally ready to be interfaced with the rest of components and the grid.

3.2.2 DC/DC Converter

The DC/DC converter corresponds to a boost converter (BC) shown in Fig. 3.4. The main task of a BC is to maintain the output voltage v_{out} at a desired level, considering that the input voltage v_{in} and load may fluctuate. In the BC, the output voltage is always higher than the input voltage. When the switch is *on*, the diode is reverse biased, thus isolating the output stage. The input supplies energy to the inductor. When the switch is *off*, the output stage receives energy from the inductor as well as from the input. The switch is controlled by a pulse-with modulation (PWM) scheme in which the duty ratio d, defined as,

$$\mathrm{d} = \mathrm{T_{on}}/\mathrm{T_s} \tag{3.8}$$

is adjusted as required [Mohan *et al.* 2001].

In (3.8), T_s represents the BC switching period, defined as the inverse of the switching frequency F_s, normally set at several kHz [Luo and Ye 2004]; T_{on} is the time in which the switch remains in *on* state within a switching period. The conduction time of the diode complements the conduction time of the switch.

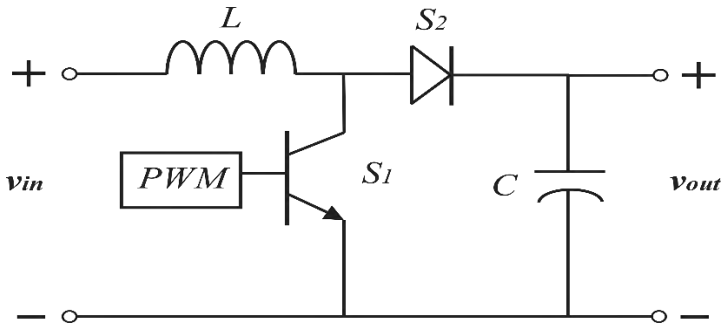

Fig. 3.4 Boost converter topology.

For the PV generation system, it is desired that the PV array works at MPP; v_{in} of the BC (equal to the output voltage of the PV array) must be equated to V_{MPP} by adjusting d.

Since the PV array depends on environmental conditions, V_{MPP} is variable. There are several MPPT algorithms; the most popular are the perturb and observe (P&O) and the incremental conductance (InC) methods [Rashid 2011]. Since this contribution ultimately centers on the periodic steady state operation condition, it is assumed that the PV array works at the MPP by adopting the P&O method. Furthermore, the PV system is a non-feedback system, i.e., the output of the system has no influence or effect on the control action of the input signal. In other words, is an open-loop system.

3.2.3 DC/AC Converter

Fig. 3.5 shows a DC/AC converter. The main objective of a DC/AC converter is to generate a sinusoidal AC output voltage, whose magnitude and frequency can both be controlled. It can be observed from Fig. 3.5 that the DC/AC converter corresponds to a single-phase full-bridge inverter. The switching actions at the DC/AC converter are controlled by a PWM scheme with unipolar voltage switching [Mohan *et al.* 2001].

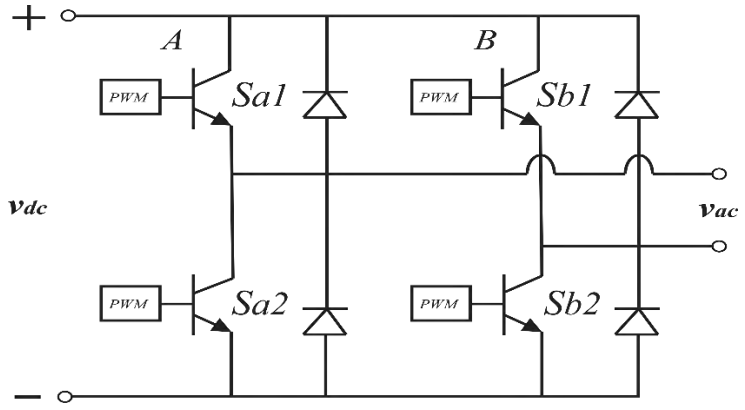

Fig. 3.5 Single-phase full-bridge inverter.

Here, the switches in the legs A and B of the full-bridge inverter are controlled separately by comparing the triangular waveform v_{tri} (which establishes the switching frequency of the inverter switches) with two sinusoidal signals $v_{control}$ and $-v_{control}$ (which sets the desired fundamental frequency of the inverter output voltage) as shown in Fig. 3.6.

In Fig. (3.6) the peak value of $v_{control}$ (the same for $-v_{control}$) is related to v_{tri} by modulation ratio m_a, calculated as:

$$m_a = \frac{v_{control}}{v_{tri}} \tag{3.9}$$

It is noted that m_a corresponds also to the ratio between the magnitude of the fundamental component of the output voltage v_{ac} and the magnitude of the input voltage v_{dc}. The frequency of v_{tri} is fixed at several kHz, and determines the order of the harmonics of v_{ac} [Mohan *et al.* 2001]. Harmonics in v_{ac} appears as sidebands centered at every two times the frequency modulation ratio m_f, given by:

$$m_f = \frac{f_s}{f_0} \tag{3.10}$$

Where f_s is the switching frequency and f_0 is the ac-system frequency.

In the unipolar PWM voltage switching scheme applied to the VSI, the control for leg A is independent of the control of leg B. For leg A, when $v_{control} < v_{tri}$, S_{a1} is turned on, otherwise is turned off (S_{a2} is always complementary to S_{a1}). The same rule governs the control of leg B, but using $-v_{control}$ instead of $v_{control}$.

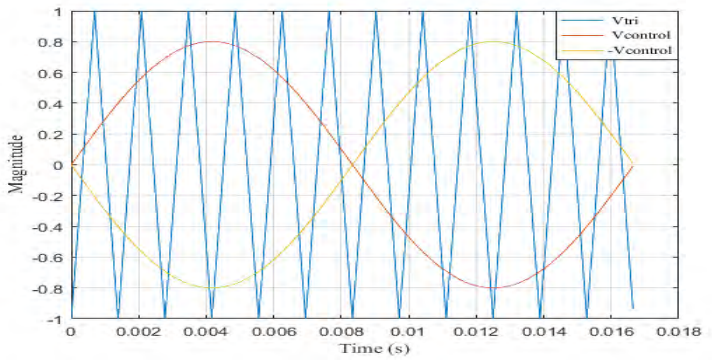

Fig. 3.6 Sinusoidal PWM for unipolar voltage switching.

As an illustrative example, consider the control of a VSI using $f_0 = 60$ Hz, $m_a = 0.8$, $m_f = 12$, and $v_{dc} = 1$. The obtained switching function s_{a1} is shown in Fig. 3.7.

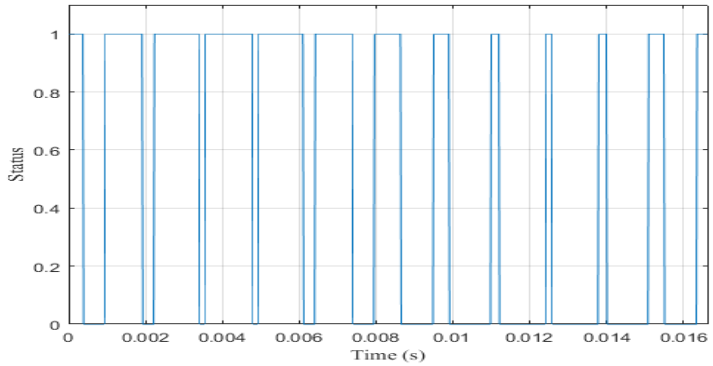

Fig. 3.7 Switching function s_{a1}.

The output voltage (v_{ac}) for this case is shown in Fig. 3.8.

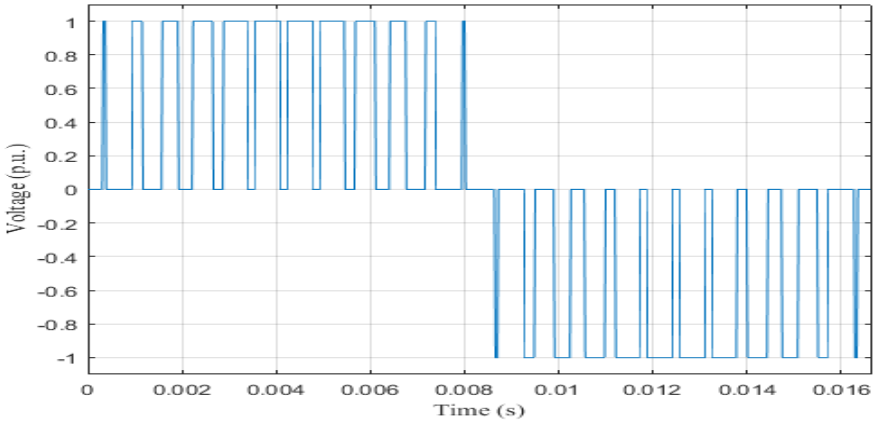

Fig. 3.8 Output voltage v_{ac}.

3.3 DAE Representation.

Fig. 3.9 shows a single-phase grid-connected PV generation system. It consists on a voltage source, a battery bank, five transmission lines, two linear loads, and the PV generation system. Fig. 3.10 shows the equivalent circuit of a single-phase grid-connected PV generation system. The dynamic operation of the system is represented by twelve DAEs, i.e., six differential equations and six algebraic. The voltage at the capacitors and the currents in the inductors where chosen as state variables.

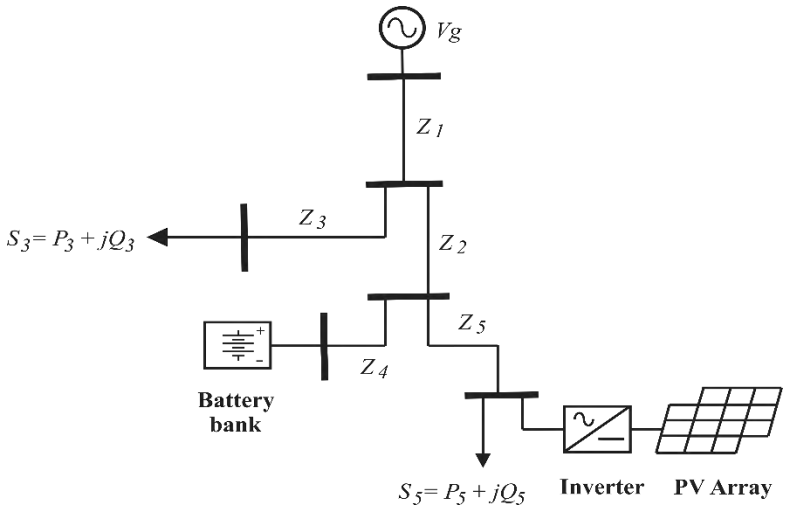

Fig. 3.9 Microgrid supplied by a PV source.

The system of DAEs is presented below:

- Differential equations.

$$\frac{d}{dt}\mathrm{v_{pv}} = -\frac{\mathrm{v_{pv}}}{\mathrm{C_{pv}R_{pv}}} - \frac{\mathrm{i_L}}{\mathrm{C_{pv}}} + \frac{\mathrm{V_{DC}}}{\mathrm{C_{pv}R_{pv}}} \tag{3.11}$$

$$\frac{d}{dt}\mathrm{i_L} = \frac{\mathrm{v_{pv}}}{\mathrm{L}} - \frac{\mathrm{v_c}}{\mathrm{L}}\mathrm{s_2} \tag{3.12}$$

$$\frac{d}{dt}\mathrm{v_c} = \frac{\mathrm{i_L}}{\mathrm{C}}\mathrm{s_2} - \frac{\mathrm{i_{fc}}}{\mathrm{C}}\mathrm{s_i} \tag{3.13}$$

$$\frac{d}{dt}\mathrm{i_{fc}} = \frac{\mathrm{v_c}}{\mathrm{L_{fc}}}\mathrm{s_i} - \frac{\mathrm{R_{fc}+R_d}}{\mathrm{L_{fc}}}\mathrm{i_{fc}} - \frac{\mathrm{v_{cf}}}{\mathrm{L_{fc}}} + \frac{\mathrm{R_d}}{\mathrm{L_{fc}}}\mathrm{i_{pcc}} \tag{3.14}$$

$$\frac{d}{dt}\mathrm{v_{cf}} = \frac{\mathrm{i_{fc}}}{\mathrm{C_f}} - \frac{\mathrm{i_{pcc}}}{\mathrm{C_f}} \tag{3.15}$$

$$\frac{d}{dt}\mathrm{v_{c5}} = \frac{\mathrm{i_5}}{\mathrm{C_5}} \tag{3.16}$$

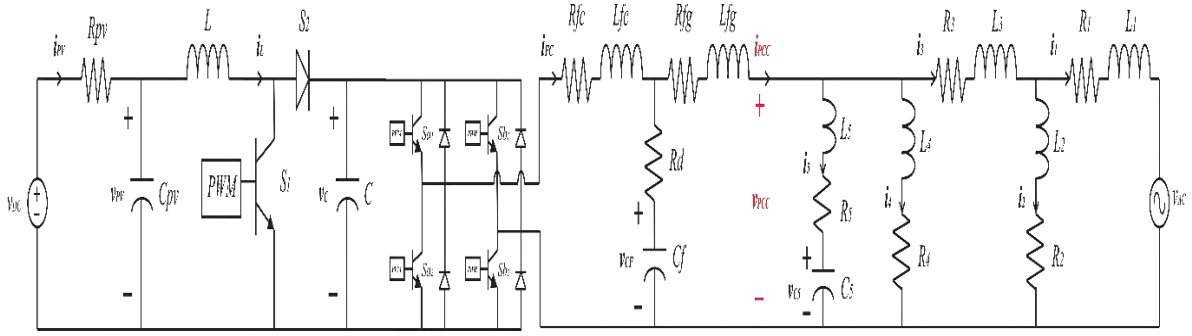

Fig. 3.10 Equivalent circuit of the microgrid supplied by a PV source.

- Algebraic equations.

$$\frac{d}{dt}\mathrm{i_{pcc}} = \frac{\left(\mathrm{D_3}-\frac{\mathrm{B_3}\left(1+\frac{\mathrm{L_1}}{\mathrm{L_2}}\right)}{\left(\mathrm{L_3}+\frac{(\mathrm{L_2}+\mathrm{L_3})\mathrm{L_1}}{\mathrm{L_2}}\right)}\right)}{\left(-1-\left(\frac{\mathrm{L_4}}{\mathrm{L_5}}+1\right)\left(\frac{\mathrm{L_{fg}}}{\mathrm{L_4}}\right)-\frac{\mathrm{L_{fg}}\left(1+\frac{\mathrm{L_1}}{\mathrm{L_2}}\right)}{\left(\mathrm{L_3}+\frac{(\mathrm{L_2}+\mathrm{L_3})\mathrm{L_1}}{\mathrm{L_2}}\right)}\right)} \tag{3.17}$$

$$\frac{d}{dt}\mathrm{i_5} = \frac{\mathrm{L_4}}{\mathrm{L_5}}\left(\frac{d}{dt}\mathrm{i_4}\right) - \frac{\mathrm{C1}}{\mathrm{L_5}} \tag{3.18}$$

$$\frac{d}{dt}\mathrm{i_4} = \frac{\mathrm{E}}{\mathrm{L_4}} - \frac{\mathrm{L_{fg}}}{\mathrm{L_4}}\left(\frac{d}{dt}\mathrm{i_{pcc}}\right) + \frac{\mathrm{C1}}{\mathrm{L_4}} \tag{3.19}$$

$$\frac{d}{dt}i_3 = \frac{d}{dt}\mathrm{i_2} + \frac{d}{dt}\mathrm{i_1} \tag{3.20}$$

$$\frac{d}{dt}\mathrm{i_2} = \frac{\mathrm{L_1}}{\mathrm{L_2}}\left(\frac{d}{dt}\mathrm{i_1}\right) - \frac{\mathrm{A}}{\mathrm{L_2}} \tag{3.21}$$

$$\frac{d}{dt}\mathrm{i_1} = \frac{\mathrm{B_3}-\mathrm{L_{fg}}\left(\frac{d}{dt}\mathrm{i_{pcc}}\right)}{\left(\mathrm{L_3}+\frac{(\mathrm{L_2}+\mathrm{L_3})\mathrm{L_1}}{\mathrm{L_2}}\right)} \tag{3.22}$$

where:

$$A = i_2 R_2 - i_1 R_1 - v_{AC}$$

$$B = R_4 i_4 - R_3 i_3 - R_2 i_2$$

$$C1 = R_5 i_5 + v_{C5} - R_4 i_4$$

$$E = R_d\left(i_{fc} - i_{pcc}\right) + v_{cf} - R_{fg} i_{pcc} - R_5 i_5 - v_{C5}$$

$$B3 = B + \frac{(L_2 + L_3)}{L_2} A + C1 + E$$

$$D3 = -\left(\frac{L_4}{L_5} + 1\right)\frac{E}{L_4} - \left(\frac{L_4}{L_5} + 1\right)\left(\frac{C1}{L_4}\right) + \frac{C1}{L_5} + \frac{A}{L_2}$$

3.4 Efficient TD Solution Using the Numerical Differentiation Method

The ND method can be applied to efficiently obtain the periodic steady state of a microgrid with PV energy sources. In principle, a nonlinear power network/component can be mathematically modeled by a set of first-order DAEs and using some integration routine, such as the TR or Fourth-Order Runge-Kutta (RK4) algorithm [Balagurusamy 1999], the periodic steady state solution is obtained. This conventional process is known as "brute force" (BF) approach [Parker and Chua 1989] and can be inefficient. It may require of a considerable time and computer effort. However, TD solution can be significantly accelerated to obtain the periodic steady state solution with the use of Newton type methods [Semlyen and Medina 1995], [Medina *et al.* 2013].

The mathematical model of DAEs is represented by state space equation,

$$\dot{\mathbf{x}} = [\mathbf{A}]\mathbf{x} + [\mathbf{B}]\mathbf{u} \tag{3.23}$$

The extrapolation to the limit cycle of the state vector represented by $\mathbf{x}^{\infty}$ can be calculated as in [Semlyen and Medina 1995], i.e.,

$$\mathbf{x}^{\infty} = \mathbf{x}^{i} + \mathbf{C}(\mathbf{x}^{i+1} - \mathbf{x}^{i}) \tag{3.24}$$

$$\mathbf{C} = (\mathbf{I} - \boldsymbol{\Phi})^{-1} \tag{3.25}$$

$$\boldsymbol{\Phi} = \partial \mathbf{x}(t + T) / \partial \mathbf{x}(t) \tag{3.26}$$

where:

$\mathbf{x}^i$ is the state vector at the beginning of the base cycle.

$\mathbf{x}^{i+1}$ is the state vector at the end of the base cycle.

$\mathbf{C}$ is the iteration matrix.

$\mathbf{\Phi}$ is the state transition matrix.

$\mathbf{I}$ is the unit matrix.

T is the fundamental frequency period.

The $\mathbf{\Phi}$ matrix can be approximated using finite-difference derivative as

$$\mathbf{\Phi} \approx \Delta\mathbf{x}(t + T)/\Delta\mathbf{x}(t) \tag{3.27}$$

The identification of $\mathbf{\Phi}$ is detailed as follows: a base cycle $\mathbf{x}(t)$ is obtained through the numerical integration of (3.23) using the BF method during several cycles starting from a determined initial condition (e.g., zero condition). Usually, the number of cycles comprises the initial transient. A base cycle can be seen as the last cycle of this initial transient period. Then, the base cycle is sequentially perturbed with a small value at the beginning of the cycle for each state variable. The difference between the base cycle and the perturbed base cycle at the end of the cycle is then evaluated to obtain $\Delta\mathbf{x}^{i+1} = \mathbf{x}^{i+1} - \mathbf{x}^i$ for all the state variables. This allows the sequential identification of the state transition matrix by columns.

With $\mathbf{\Phi}$ identified, the iteration matrix $\mathbf{C}$ can be evaluated using (3.25). Finally, at this point the state vector at the limit cycle can be evaluated using (3.24). It represents the limit cycle estimation of the state vector.

In other words, ND computes $\mathbf{\Phi}$ using a column by column process. The *k*th column of $\mathbf{\Phi}$ is Φ_k, for $k = 1, 2, \ldots n$. This column can be computed by perturbing the *k*th state, i.e., let $\mathbf{x}(t) \rightarrow \mathbf{x}(t) + \Delta\mathbf{x}_k(t)$ and compute $\mathbf{x}(t+T) + \Delta\mathbf{x}_k(t+T)$ by numerical integration of (3.23) over one period with the initial condition $\mathbf{x}(t) \rightarrow \mathbf{x}(t) + \Delta\mathbf{x}_k(t)$.

Notice that if $\Delta\mathbf{x}_k(t)$ is equal to εU_k, being ε a small real number, e.g., 10^{-6}, and U_k the *k*th column of a identity matrix of dimension *n*, for $k = 1, 2, \ldots n$, then, by considering (3.27) we obtain,

$$\Delta\mathbf{x}_k(t+T) = \mathbf{\Phi}\varepsilon U_k \tag{3.28}$$

and consequently

$$\Delta\mathbf{x}_k(t+T) = \varepsilon\Phi_k \tag{3.29}$$

Therefore

$$\Phi_k = \Delta x_k(t+T)/\varepsilon \tag{3.30}$$

Each column of $\mathbf{\Phi}$ can be computed with (3.30). All *n* states of the system (3.23) must be perturbed separately in order to compute the *n* columns of the sensitivity matrix. Note that *n+1* cycles must be computed before we can apply (3.24).

3.4.1 Variants of Implementation

The identification of the $\mathbf{\Phi}$ matrix is the most computationally demanding task during the iterative TD location of the limit cycle. Different implementation strategies can be explored for the efficient solution of the microgrid with PV energy sources using the ND method. If $\mathbf{\Phi}$ and $\mathbf{C}$ are updated at each iteration step using (3.25) and (3.26), a Newton Process of quadratic convergence to the limit cycle of the state variables results [Semlyen and Medina 1995]. On the other hand, it becomes a linearly convergent process if $\mathbf{\Phi}$ and $\mathbf{C}$ are kept constant after the first evaluation using (3.25) and (3.26).

However, the solution process is expected to be significantly faster than the first approach, since a repetitive identification of $\mathbf{\Phi}$ is avoided.

3.5 Cubic Spline Interpolation

Once the ND method has obtained the steady state solution using the fewest number of possible time steps, it does not represent the final solution and different order harmonics may appear. To avoid this, it is necessary to use an interpolation method that estimates data points using a mathematical function that minimizes overall surface curvature, resulting in a surface that passes exactly through the input points. In this thesis, CSI is used. The objective of CSI process is to derive a third-order polynomial for each interval of data points [Chapra and Canale 2010]. The polynomial for each interval can be represented by its general form,

$$f_i(x) = a_i x^3 + b_i x^2 + c_i x + d_i \tag{3.31}$$

Fig. 3.11 helps to explain the notation used to derive cubic splines. The first step in the derivation [Cheney and Kincaid 2008] is based on the observation that since each pair of knots is connected by a cubic, the second derivative within each interval is a straight line. Equation (3.31) can be differentiated twice to verify this observation. On this basis, the second derivatives can be represented by a first-order Lagrange interpolating polynomial:

$$f_i''(x) = f_i''(x_{i-1})\frac{x-x_i}{x_{i-1}-x_i} + f_i''(x_i)\frac{x-x_{i-1}}{x_i-x_{i-1}} \tag{3.32}$$

where $f_i''(x)$ is the value of the second derivative at any point x within the i*th* interval. Thus, this equation is a straight line connecting the second derivative at the first knot $f''(x_{i-1})$ with the second derivative at the second knot $f''(x_i)$.

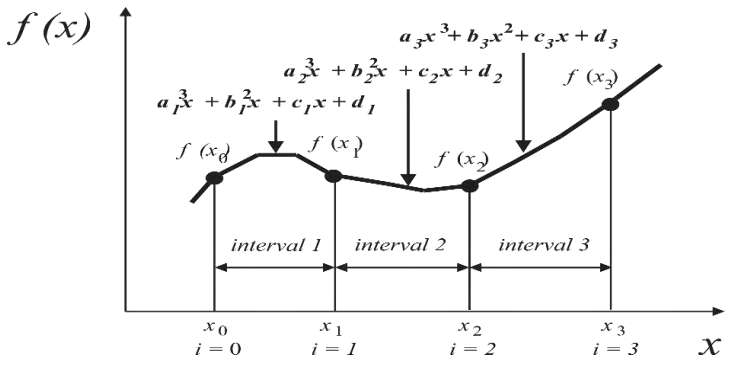

Fig. 3.11 Notation used to derive cubic splines.

Next, (3.32) can be integrated twice to yield an expression for $f_i(x)$. However, this expression will contain two unknown constants of integration. These constants can be evaluated by invoking the function-equality conditions, i.e., f(x) must equal $f(x_{i-1})$ at x_{i-1} and f(x) must equal $f(x_i)$ at x_i. By performing these evaluations, the following cubic equation results:

$$f_i(x) = \frac{f_i''(x_{i-1})}{6(x_i - x_{i-1})}(x_i - x)^3 + \frac{f_i''(x_i)}{6(x_i - x_{i-1})}(x - x_{i-1})^3 + \left[\frac{f(x_{i-1})}{x_i - x_{i-1}} - \frac{f''(x_{i-1})(x_i - x_{i-1})}{6}\right] + \left[\frac{f(x_i)}{x_i - x_{i-1}} - \frac{f''(x_{i-1})(x_i - x_{i-1})}{6}\right] \quad (3.33)$$

Admittedly, this relationship is a much more complicated expression for the cubic spline for the i*th* interval than, say, (3.31). However, notice that it contains only two unknown "coefficients", i.e., the second derivatives at the beginning and at the end of the interval $f''(x_{i-1})$ and $f''(x_i)$. Thus, if we can determine the proper second derivative at each knot, (3.33) is a third-order polynomial that can be used to interpolate within the interval.

The second derivatives can be evaluated by invoking the condition that the first derivatives at the knots must be continuous:

$$f_i'(x_i) = f_{i+1}'(x_i) \quad (3.34)$$

Equation (3.33) can be differentiated to give an expression for the first derivative. If this is done for both the (i-1)*th* and the i*th* intervals and the two results are set equal according to (3.34), the following relationship results:

$$(x_i - x_{i-1})f''(x_{i-1}) + 2(x_{i+1} - x_{i-1})f''(x_i) + (x_{i+1} - x_i)f''(x_{i+1}) = \frac{6}{x_{i+1} - x_i}[f(x_{i+1}) - f(x_i)] + \frac{6}{x_i - x_{i-1}}[f(x_{i-1}) - f(x_i)] \quad (3.35)$$

If (3.35) is written for all interior knots, *n-1* simultaneous equations result with *n+1* unknown second derivatives. However, since this is a natural cubic spline, the second derivatives at the end knots are zero and the problem reduces to *n-1* equations with *n-1* unknowns. In addition, notice that the system of equations will be tridiagonal. Thus, not only have we reduced the number of equations but we have also add them in a form that is extremely easy to solve.

3.6 General Time Domain Solution Scheme

The flowchart of the solution method to obtain the periodic steady state of microgrids with PV energy sources is shown in Fig. 3.12. It is basically composed by five blocks, whose function are as follows: the first block reads the parameters of the microgrid and the PV generation system, the second block obtains the Thevenin equivalent circuit of the PV array, the third block is based on the circuit of Fig 3.1, where the PV array is replaced by the corresponding Thevenin equivalent, finds the set of DAEs. The DAE representation of the grid connected PV generation system is efficiently solved with the ND method in the fourth block. Finally, the fifth block reconstructs the steady state waveform using the CSI method.

3.7 Test Case of PV System in TD

The periodic steady state solution of the single-phase grid-connected PV generation system of Fig. 3.10 is obtained in time domain framework. The solution is obtained using the BF and ND combined with CSI (ND-CSI) methods.

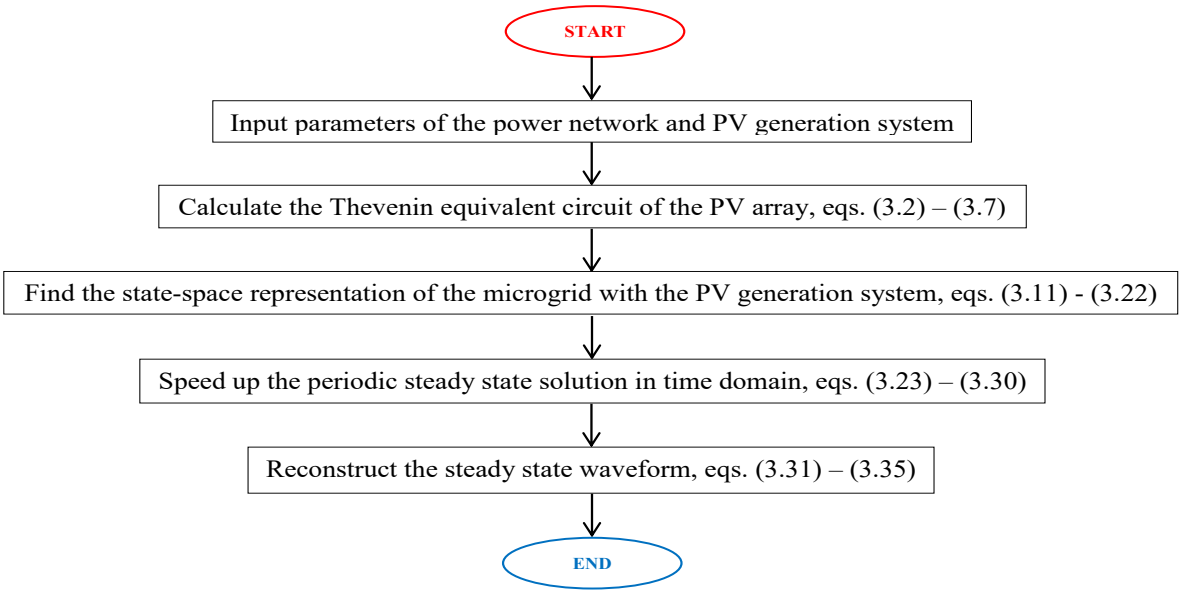

Fig. 3.12 Flowchart of the ND-CSI method.

For the first case, the BF procedure is evaluated with a sampling time-step of 0.1 μs. For the second case, ND obtains the periodic steady state with a sampling time-step of 2.5 μs. Then, CSI is used just once to reconstruct the waveform. The criterion for convergence of the state variables has been defined as 10^{-4}.The corresponding parameters are contained in Table 3.1. The PV array is solved for standard test conditions (STC), i.e., irradiance of 1000 W/m^2 and temperature of 25°C. The PV system operates at the MPP.

Table 3.1 Data for grid-connected PV generation system.

PV array at STC		
N_S	17	Number of modules connected in series
N_P	2	Number of modules connected in parallel
V_{oc}	21.47 V	Open-circuit voltage per module
I_{sc}	7.6 A	Short-circuit current per module
V_{mpp}	17.1 V	Voltage at MPP per module
I_{mpp}	7.1 A	Current at MPP per module
P_{max}	121.41 W	Maximum power per module
n_S	28	Number of cells connected in series per module
k_i	0.00502 A/°C	Temperature correction factor for current
k_v	-0.08 V/°C	Temperature correction factor for voltage
a	1.3	Ideality factor of diode
DC/DC Converter		
C_{pv}	5500 μF	Capacitance
L	9 mH	Inductance
C	2200 μF	Capacitance
F_s	10 kHz	Switching Frequency
DC/AC Converter		
F_{SW}	25 kHz	Switching Frequency
m_a	0.9	Modulation index
Filter		
R_{fc}	1 mΩ	Resistance
L_{fc}	0.3 mH	Inductance

R_{fg}	1 mΩ	Resistance
L_{fg}	0.15 mH	Inductance
R_d	2 Ω	Resistance
C_f	2.2 μF	Capacitance
Microgrid		
V_{AC}	230 V	Voltage (RMS)
R_1	1 Ω	Resistance
R_2	33 Ω	Resistance
R_3	1 Ω	Resistance
R_4	33 Ω	Resistance
R_5	1 Ω	Resistance
L_1	1 mH	Inductance
L_2	0.17 H	Inductance
L_3	1 mH	Inductance
L_4	0.17 H	Inductance
L_5	1 mH	Inductance
C_5	220 μF	Capacitance

The resultant variables of the PV array are obtained via the procedure described in section 3.2.1 and presented in Table 3.2.

Based on the parameters of Table 3.1, the V-I and P-V curves of the PV array are presented in Figs. 3.13 and 3.14. The V-I and P-V curves of the PV array are a scale-up of the curves of the PV module. This is because the association of PV modules provides a higher current and voltage output.

Table 3.2 Variables calculated for the PV array.

Key points of V-I curve of PV array		
V_{OC}	365 V	Open-circuit voltage (total)
I_{SC}	15.2 A	Short-circuit current (total)

V_{MPP}	290.8 V	Voltage at MPP (total)
I_{MPP}	14.2 A	Current at MPP (total)
P_{MAX}	4129.4 W	Maximum power (total)
Parameters for Norton Equivalent		
R_S	2.0 Ω	Series resistance
R_P	2.172 kΩ	Parallel resistance
I_{TH}	14.33 A	Norton current
R_{TH}	2.174 kΩ	Norton resistance

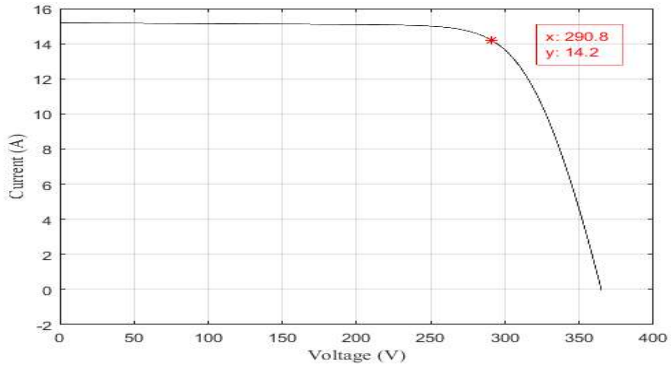

Fig. 3.13 V-I curve.

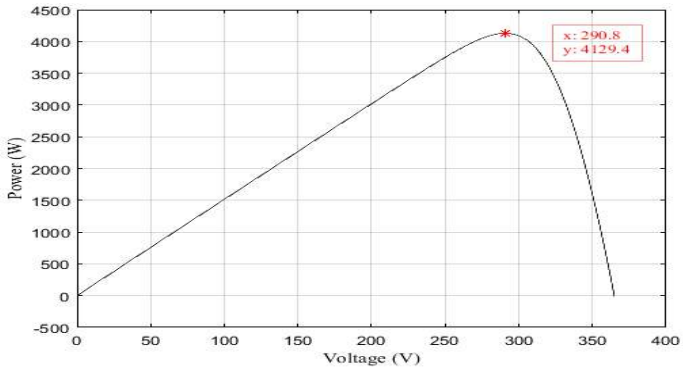

Fig. 3.14 P-V curve.

Fig. 3.15 shows the solution process to the periodic steady state of the current waveform at PCC with the ND-CSI. Five initial cycles and a base cycle were obtained before applying the ND method. One cycle of the periodic steady state solution is shown.

The current waveform at PCC obtained with the BF, ND-CSI, and PSCAD/EMTDC methods is illustrated in Fig. 3.16. An excellent agreement between responses can be observed. The corresponding comparison in harmonic content is shown in Fig. 3.17. Please notice that the harmonic distortion of the waveform is mainly due to the presence of third, fifth and seventh harmonics. The magnitude of the third harmonic is above the limit allowed by harmonic standards [IEEE Std 519-1992]. Again, a close agreement between the responses obtained with the BF, ND-CSI, and PSCAD/EMTDC are shown.

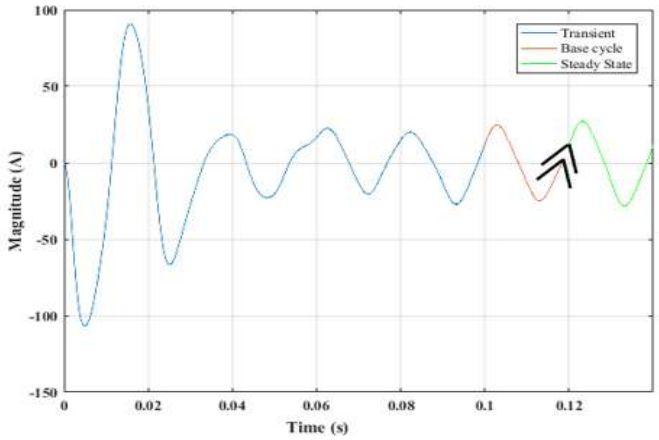

Fig. 3.15 Current at the PCC.

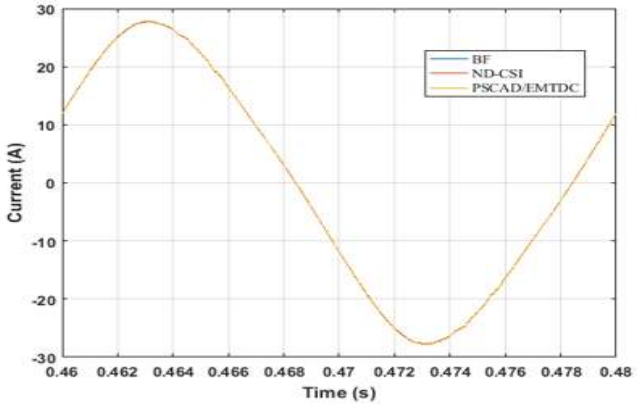

Fig. 3.16 Steady state current at the PC.

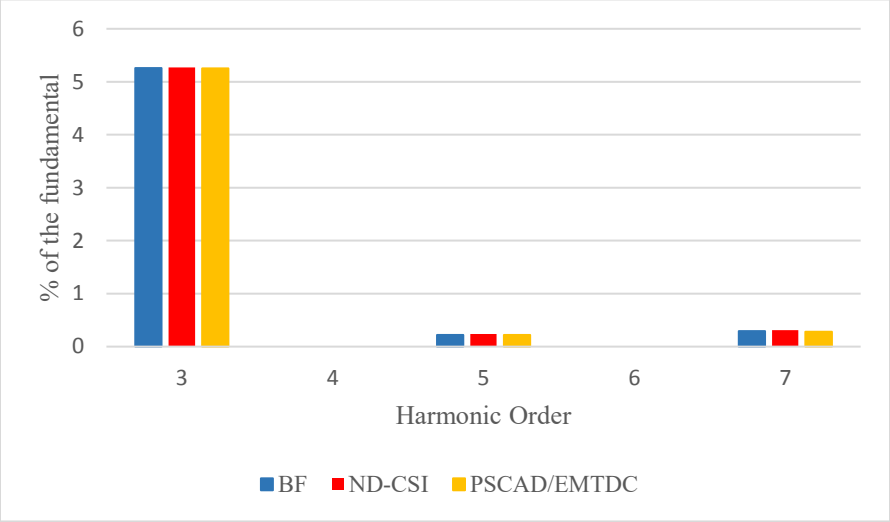

Fig. 3.17 Current harmonic content.

Table 3.3 shows the converged values of d and of the DC components (averages) of voltage and current at the PV array terminals. Table 3.3 concludes that the obtained values agree with the MPP as given in Table 3.2. Also, Table 3.3 reports the THD and powers at the PCC obtained with the BF and ND-CSI methods, respectively. Please observe that the maximum error between responses is negligible, i.e., it is only 0.02% for the THD in i_{pcc}.

The algorithm used in this research was implemented on AMD A8-6410 APU processor with AMD Radeon R5 Graphics, 2 GHz, and 6 GB of DDR3 onboard memory. Table 3.4 presents the variants of implementation of the ND method. The CPU time needed by the ND-CSI with Φ variable method to obtain the periodic steady state solution was 35 ms while by the ND-CSI with Φ constant procedure was 17 ms. In other words, the ND with $\mathbf{\Phi}$ constant is on average 2 times faster than the ND with $\mathbf{\Phi}$ variable. Also, the ND with $\mathbf{\Phi}$ constant is 20 times faster than BF method.

Table 3.3 Simulation results of TD case.

PV array			
V_{pv0}	290.93	DC component of voltage at PV terminals	
I_{pv0}	14.20	DC component of current at PV terminals	
Boost converter			
d	0.277	Duty Ratio	
Point of common coupling			
	BF	*ND-CSI*	
THD in v_{pcc}	1.16 %	1.17 %	Total harmonic distortion
THD in i_{pcc}	5.27 %	5.29 %	Total harmonic distortion
S	4.7715 kVA	4.7735 kVA	Apparent power
P	4.1350 kW	4.1370 kW	Active power
PF	0.8667	0.8669	Power factor

In terms of the number of full time domain cycles (NFC) required for the convergence to the limit cycle, the BF method took 38, the ND-CSI with **Φ** variable took 18, and ND-CSI with **Φ** constant took 30.

Table 3.4 Comparison of solution methods.

	BF	**Φ** *variable*	**Φ** *constant*
Time (ms)	348	35	17
NFC	38	18	30

Finally, two fast and efficient methodologies for the simulation of the periodic steady state response of power networks under non-sinusoidal conditions in the TD are presented. The firs one is shown in Section 3.8 and uses the TR, DN, and CSI algorithms. The second one is shown in Section 3.9 and uses the same three methods as the previous one, but a parallel processing technique based on multi-CPUS and multi-GPUS is added.

3.8 Harmonic Propagation in TD

The three-bus test system of Figure 3.18 has been solved with the BF, the ND, and with the ND-CSI. For the first case, ND uses 1024 time steps to integrate a complete period of time of the equations describing the system. For the second case, the ND uses the fewest possible time steps to obtain the periodic steady state. Then, CSI is used to reconstruct the waveform.

The system of Fig. 3.18 has two magnetizing branches connected at bus two and three, respectively. Two capacitors connected at the same buses, three resistors and inductors (transmission lines), and a voltage source. The dynamic operation of the system is represented by seven differential equations. The voltage at the capacitors, the flux linkage of the magnetizing branches and the currents in the inductors were chosen as state variables.

Fig. 3.19 shows part of the process to reach the steady state current at bus two. Three initial cycles and a base cycle, before using the ND method, and two steady state cycles. This bus was chosen due to the fact it has a nonlinear element connected.

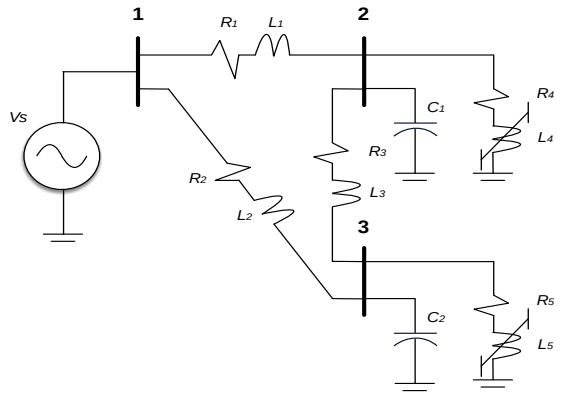

Fig. 3.18 Three-bus test system.

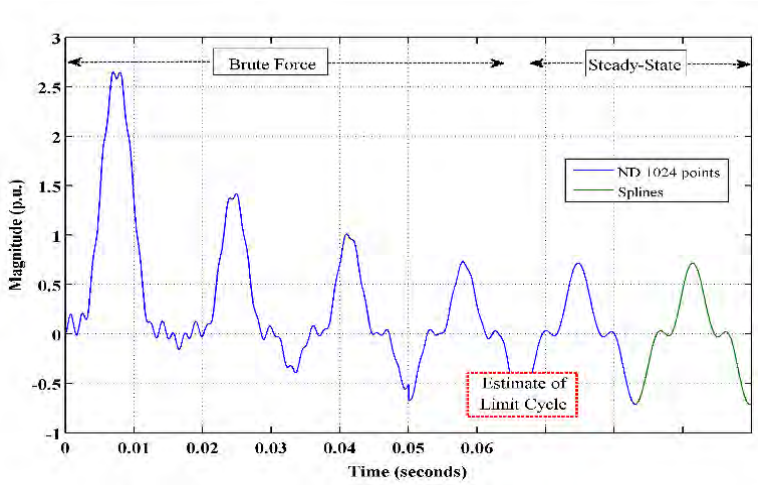

Fig. 3.19 Behavior of the current at bus two.

Fig. 3.20 is a zoom of half cycle of the steady state current at bus two. The ND-CSI method (with the fewest possible time steps) is an excellent alternative to the ND method with 1024 time steps.

Fig. 3.21 shows the harmonic spectrum using the FFT. Fig. 3.21 shows the close agreement achieved between responses obtained with both methods. Twenty harmonics are shown, all of them in percent of the fundamental. The harmonics that most influence the distorted waveform are the third, fifth, and seventh. The magnitudes are 61.6 %, 8.2 % and 3.5%, respectively, using the ND method with 1024 time steps per cycle. On the other hand, the magnitude of the third is 62.3%, the fifth is 9.1%, and the seventh is 3.7% with the ND-CSI approach. The maximum error between responses is 0.9%.

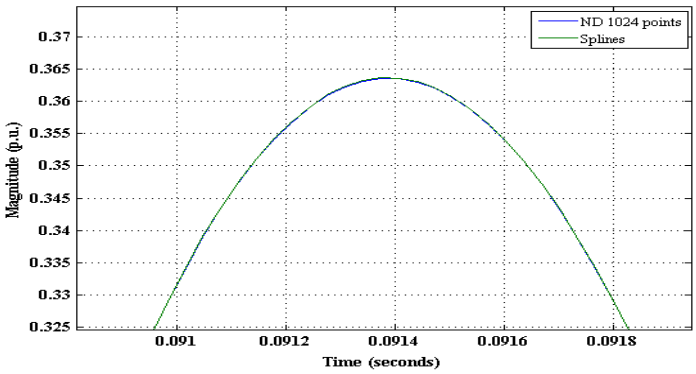

Fig. 3.20 Zoom-in of the steady state current at bus two.

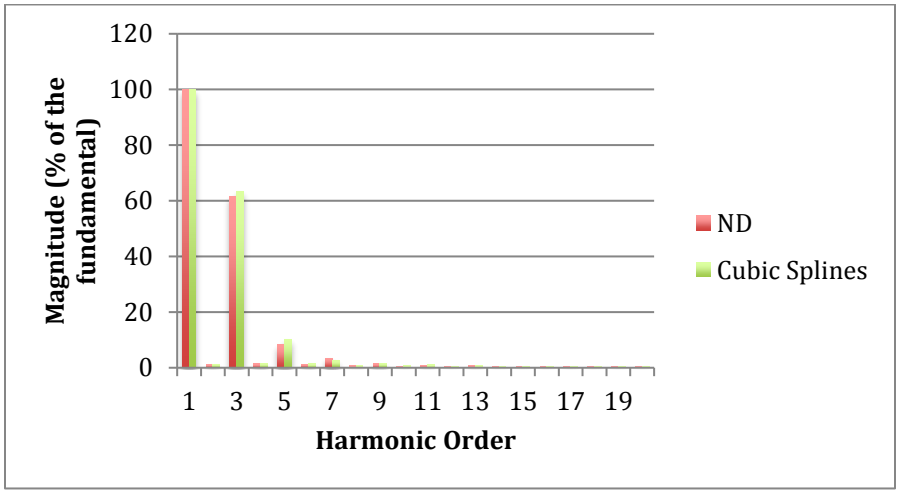

Fig. 3.21 Harmonic spectrum of Fig. 5.13.

The CPU time needed by the ND with 1024 time steps per cycle is 43 ms, and for the ND-CSI procedure is 10 ms or 4 times less.

A similar case takes place with the voltage waveform at bus 2, as shown in Fig. 3.22. Please observe that this waveform presents a low harmonic order distortion due to the capacitor connected in parallel. The harmonic spectrum is shown in Fig. 3.23. Please observe that the conventional ND and the ND combine with CSI are in close agreement.

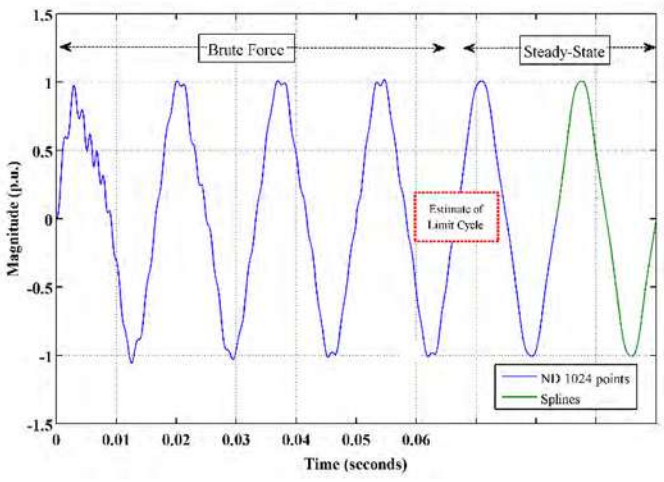

Fig. 3.22 Behavior of the voltage at bus 2.

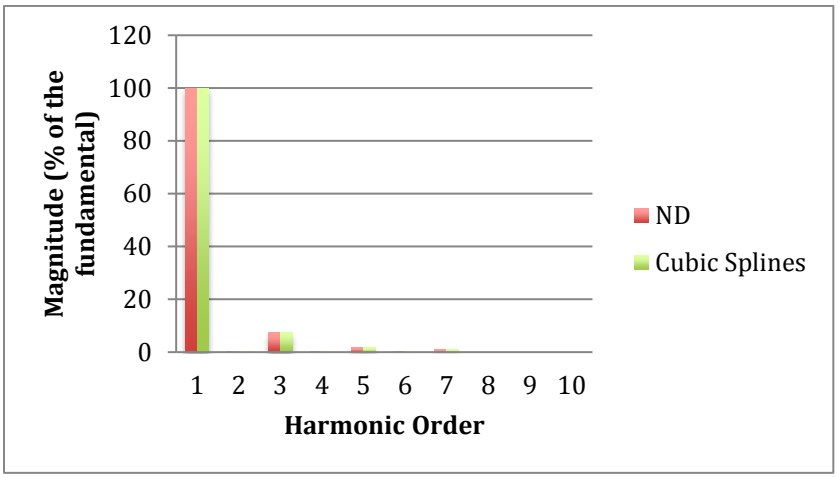

Fig. 3.23 Harmonic spectrum of Fig. 5.16.

The proposed ND-CSI method has been applied for the periodic steady state solution of larger systems. The IEEE-14 bus test system has been modified to include nonlinear loads. It has twenty transmission lines, fourteen capacitors bank, eight generators, and fourteen magnetizing branches. The state variables are related with the voltage at the capacitors banks, the flux linkage of the magnetizing branches, and the currents in the transmission lines.

The ND method uses 1024 time steps per cycle and the ND combined with CSI 256 time steps per cycle.

The BF procedure took 101 complete cycles to obtain the steady state response and the ND method 61. Table 3.5 shows the CPU time required for the periodic state solution of the modified IEEE-14 and 30 bus test systems. The second column shows the consumed time by the BF method, the third column by the ND method, and the fourth column by the ND-CSI method.

The comparison between the third and fourth columns shows the importance of using CSI. The ND-CSI method is 5 times faster than just the ND method. In addition, the comparison between the second and the fourth columns show that the ND-CSI method is almost 7 times faster than the BF method.

It is important to mention that when only the ND method (using the fewest possible time steps), without CSI is applied to find the steady state solution, different order harmonics may appear in the spectrum.

Table 3.5 CPU time in larger systems TD.

IEEE system	***BF Time (ms)***	***ND Time (ms)***	***CSI Time (ms)***
14	1,483	961	224
30	4,436	2,831	554

Figure 3.24 shows the steady state nodal current at bus 14. The graph is a comparison between the two algorithms. The waveform generated by ND method is overlapped to the obtained with the ND-CSI using 256 time steps per cycle.

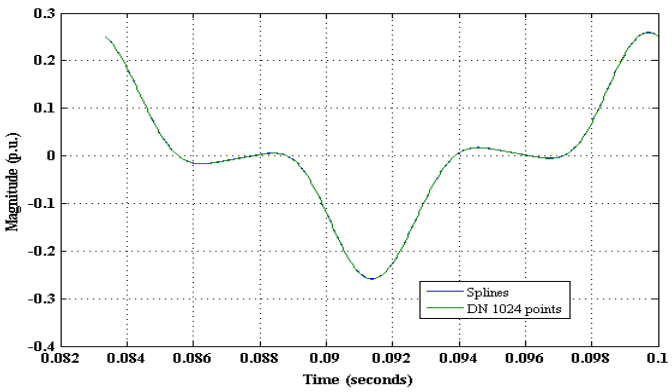

Fig. 3.24 Steady state nodal current at bus 14.

3.9 Harmonic Propagation with multi-CPU and multi-GPU in TD

The algorithm developed for this research was implemented on a Dell Precision R5500 Workstation with Intel Xeon processor, 2.2 GHz, and 6 GB onboard memory. The workstation has three GPUs connected. The Tesla C2075 with Fermi architecture, the GeForce GTX 650 with Kepler architecture, and GTX 660 with Kepler architecture. The parallel algorithm was develop by [Magaña 2016].

The Tesla C2075 features up to 448 CUDA cores, 6 GB of GDDR5 DRAM memory. The 448 CUDA cores are organized in 14 streaming multiprocessors of 32 cores each. The GeForce GTX 650 has 768 CUDA cores, 1 GB of memory. The 768 CUDA cores are organized in 4 streaming multiprocessors of 192 cores each. The GeForce GTX 660 has 1152 CUDA cores, 1.5 GB of memory. The 1152 CUDA cores are organized in 6 streaming multiprocessors of 192 cores each.

As observed, we have multiple GPUs with Fermi and Kepler architectures, so it is necessary to have at least one CPU core for each GPU. Furthermore, it is necessary to have a software to perform parallel processing techniques on the CPU and on the GPU. Figure 3.25 illustrates that OpenMP is used for the CPU and CUDA is used for the GPUs. Both platforms interact with each other through programs written in C language.

Figure 3.26 shows the sequential algorithm for the ND method with $\mathbf{\Phi}$ constant. It is composed by four blocks. The first block calculates the vectors of state variables at the beginning $\mathbf{x}^{\mathbf{i}}$ and end of the base cycle $\mathbf{x}^{\mathbf{i+1}}$, respectively. The second block is the calculation of state transition matrix $\mathbf{\Phi}$. The third block evaluates $\mathbf{C}$ using (3.24) and finally block four obtains the solution (3.25).

To reduce CPU time in the algorithm of Fig. 3.26, it is necessary to apply parallel processing techniques to each block, i.e., in all integration periods parallel processing needs to be applied (initial cycle and base cycle in block 1, $\mathbf{\Phi}$ matrix in block 2 and final cycles in block 4). The matrix inverse is calculated in block 3; part of the process can be parallelized.

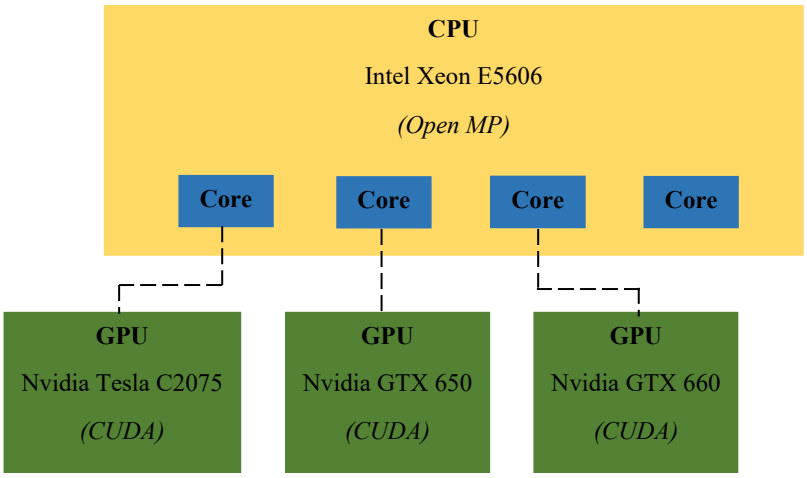

Fig. 3.25 Proposed platform.

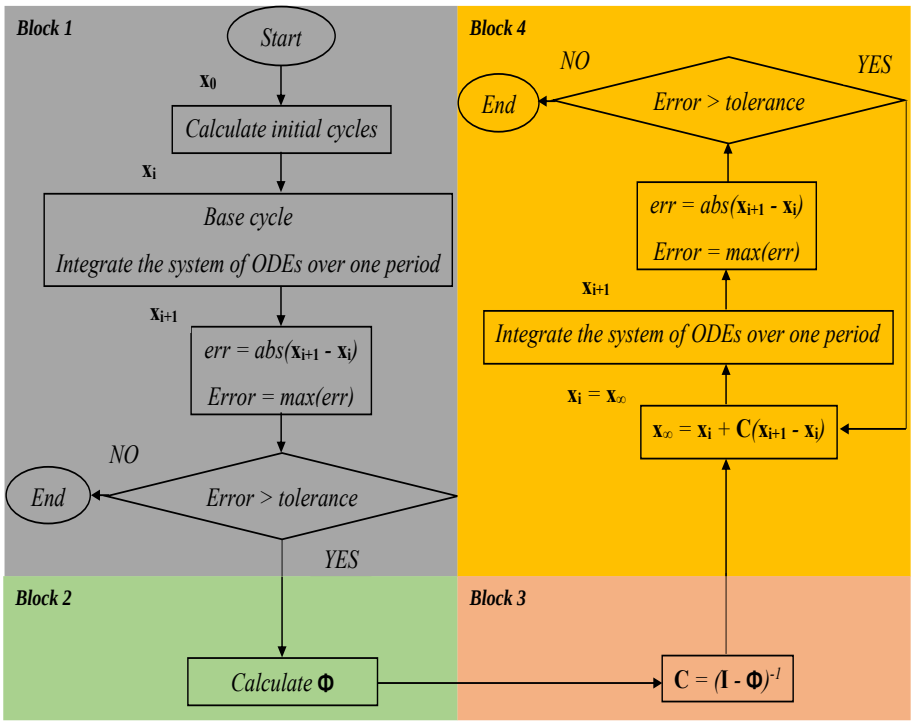

Fig. 3.26 Sequential DN Method with **Φ** constant.

On the other hand, block 2 performs the maximum computer effort since **Φ** is computed in a column-by-column process. For the computation of the column, it is necessary to make a copy of the vectors $\mathbf{x_i}$ and $\mathbf{x_{i+1}}$ from the CPU to the GPU. Each GPU will process several columns simultaneously. After all columns assigned to the GPU are processed, a copy from the GPU to CPU is made and columns are placed in the **Φ** matrix. Figure 3.27 shows the proposed algorithm for the computation of **Φ** with several CPUs and GPUs.

In addition, Fig. 3.28 shows the algorithm to increase memory efficiency in block 3. With **Φ** calculated, the solution of (2.7) is as follows:

- LU decomposition is applied to Matrix **C** (this process is done in the CPU).
- A copy of matrix **C** is made from the CPU to GPU.
- Unit matrix **B** is defined in the GPU.
- Using **Ly** = **B**, vector **y** is calculated by forward substitution by thread *n* (this process is done in the GPU).
- Using **UX** = **y**, the solution vector **X** is obtained by backward substitution.
- A copy of matrix **X** is made from GPU to CPU.

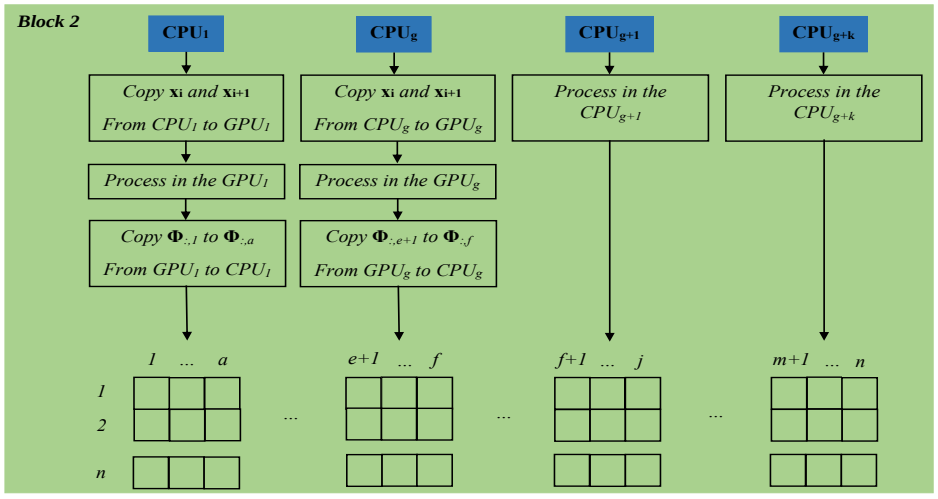

Fig. 3.27 Φ calculation with several CPUs and GPUs.

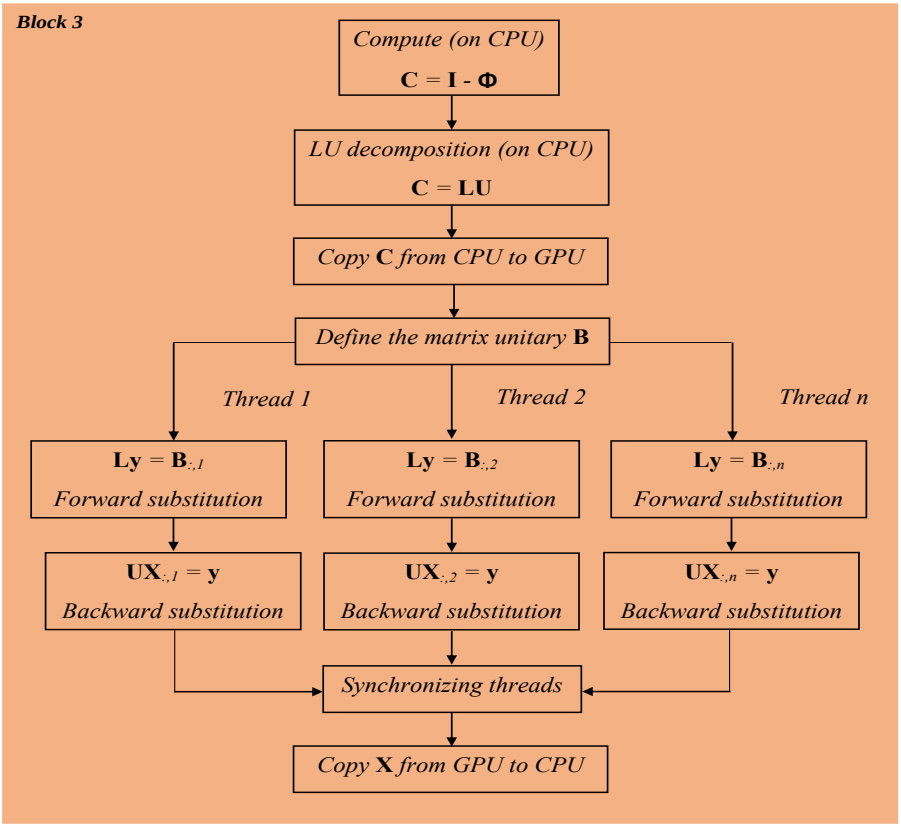

Fig. 3.28 Solution process with several CPUs and GPUs

3.10 Harmonic Propagation with Parallel-Computing in TD

The IEEE-14 bus test system have been solved with BF, ND-CSI sequential and ND-CSI parallelized algorithm. The electric power systems have been modified to include nonlinear loads, such as, magnetizing branches and arc furnaces. Both procedures use ND with the fewest possible time steps to integrate a complete period of time of the equations describing the system, and CSI to reconstruct the waveform.

The modified IEEE-14 bus test system has ten magnetizing branches, fourteen capacitor banks, twenty resistors and inductors (transmission lines), and eight generators. The dynamic operation of the system is represented by fifty six differential equations. The voltage at the capacitor banks, the flux linkage of the magnetizing branches and the currents in the inductors were chosen as state variables. It is important to mention that the system of equations were obtain through an algorithm developed by [Ramos 2007].

Fig. 3.29 shows part of the process to reach the steady state current at bus 11. Five initial cycles and a base cycle are obtained before using the ND method, and two cycles of extrapolation to the limit cycle. This bus was chosen due to the fact that it has a nonlinear element connected. Light damping for the system was assumed.

Figure 3.30 is a zoom of half cycle of the steady state current at bus 11. The parallelized ND-CSI method with 256 time steps is an excellent alternative to the BF and ND-CSI sequential.

The best way to compare these two methods (BF, and ND-CSI parallelized) is to obtain its harmonic spectrum using the Fast Fourier Transform. Please notice that this waveform presents a large harmonic distortion due to the presence of many nonlinear loads connected. The harmonics that most influence the distorted waveform are the third, fifth, and ninth, respectively. The magnitudes are 42.93%, 3.65% and 1.68%, respectively, using the BF method with 1024 time steps per cycle. On the other hand, the magnitude of the third is 42.94%, the fifth is 3.67%, and the ninth is 1.69% with the ND-CSI parallelized approach. The maximum error between responses is 0.02%. It is clear that both methods are in close agreement.

The CPU time needed by the BF with 256 time steps per cycle is 1117 ms, for the ND-CSI sequential is 678 ms, and for the ND-CSI parallelized procedure is 141 ms or 4.8 times less.

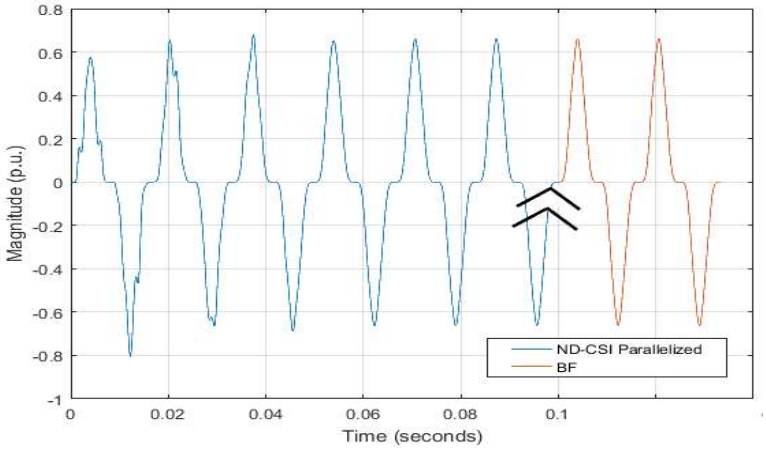

Fig. 3.29 Behavior of the current at bus 11.

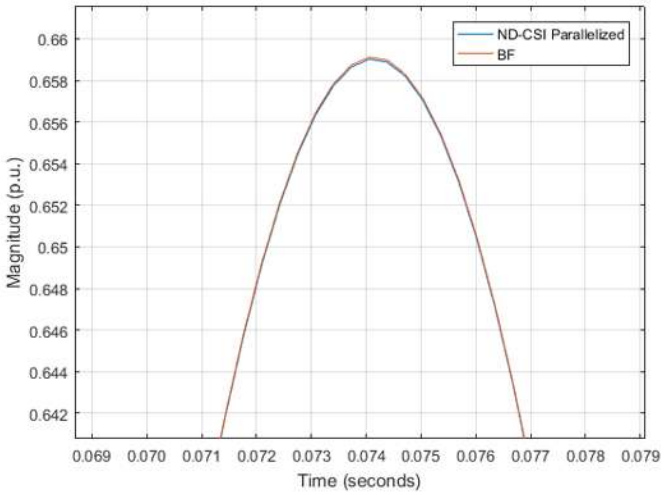

Fig. 5.30 Zoom-in of the steady state current at bus 11.

The BF, ND-CSI sequential, and the proposed ND-CSI parallelized method with 256 time steps per cycle have been applied for the periodic steady state solution of larger systems. The IEEE-30, 57, and 118 test bus systems have been modified to include nonlinear loads.

As an example, the IEEE-30 test bus system was chosen. The dynamic behavior of the system is represented by ninety-four differential equations. The state variables are related with the voltage at the capacitor banks, the flux linkage of the magnetizing branches, and the currents in the transmission lines.

The BF procedure took 161 complete cycles to obtain the steady state response and the ND-CSI parallelized method 115.

Table 3.6 shows the CPU time required for the periodic steady state solution of the modified IEEE Bus Test Systems solved with BF and ND-CSI parallelized. The second column shows the number of state variables, the third column is the consumed time by the BF method, the fourth column by the ND-CSI parallelized method, and the fifth column shows the speed up of the proposed algorithm. The comparison between the third and fourth columns shows the importance of using CSI and parallel processing techniques.

Table 3.6 CPU time in larger systems (BF *versus* ND-CSI parallelized).

IEEE system	***n***	***BF*** *Time (ms)*	***ND-CSI Parallelized*** *Time (ms)*	$\frac{\textbf{ND-CSI Parallelized}}{\textbf{BF}}$
14	56	1117	141	7.9
30	94	2335	201	11.6
57	152	3124	230	13.5
118	479	154113	1450	106.2

Table 3.7 shows the CPU time required for the periodic steady state solution of the modified IEEE Bus Test Systems solved with ND-CSI sequential and ND-CSI parallelized. Third column is the consumed time by the ND-CSI sequential method and the fourth column by the ND-CSI parallelized method. Last column shows the speed up of the proposed algorithm.

The ND-CSI parallelized method is 8.7 times faster than ND-CSI sequential for the IEEE-30 bus test system. However, the result for the best case (IEEE-118 bus test system) is that the ND-CSI parallelized algorithm is 42 times faster than the ND-CSI sequential.

Table 3.7 CPU time in larger systems (ND-CSI sequential *versus* ND-CSI parallelized).

IEEE system	***n***	***ND-CSI Sequential*** *Time (ms)*	***ND-CSI Parallelized*** *Time (ms)*	$\frac{\textbf{DN-CSI Parallelized}}{\textbf{ND-CSI Sequential}}$
14	56	678	141	4.8
30	94	1,759	201	8.7
57	152	2,829	230	12.3
118	479	61,040	1450	42.0

3.11 Conclusions

A TD methodology to assess the dynamic operation and harmonic distortion produced in microgrids with integration of PV sources has been implemented. It is based on the representation of the grid-connected PV generation system by a set of DAEs, to be solved by a numerical integration method, such as the RT or RK4 methods. The TD solution is enhanced with the combined application of extrapolation to the limit cycle based on the ND method and CSI to the voltage and current waveforms. With the proposed methodology, the TD solution can be obtained with considerably less computational effort.

The obtained results have been corroborated with those of PSCAD/EMTDC simulator, widely accepted by the power industry. It is important to mention that the PSCAD/EMTDC equivalent circuit of the single-phase grid-connected PV generation system was built using power electronic devices.

The application of parallel-computing to the periodic steady state solution in TD has been described, as well as in the harmonic propagation algorithm. A solution is always obtained and the algorithm exploits the CIM and LU Decomposition.

The implementation of parallel GPU-computing for large electrical networks has been very effective and accurate. Even for the small test system analyzed, it has shown that the parallel algorithm is faster than the sequential algorithm.

Chapter 4

Conventional and PV Systems Modelling in Frequency Domain Methodology

4.1 Introduction

Network harmonics are defined as sinusoidal voltage or current waveforms of frequencies being integer multiples of the main generated (or fundamental) frequency [Arrillaga and Watson 2004]. Harmonics can be generated by diverse nonlinear loads and sources, e.g., saturated transformers, power electronic devices, wind generators, among others. The presence of harmonics in electrical networks can produce several undesirable effects such us telephone interference, overvoltage at capacitor banks, overheating in wires, vibration of motors, system resonances, among others [Heydt 1991].

The above mentioned effects decrease the efficiency of the electrical network and the lifetime of surrounding equipment. For all these reasons, power quality analysis has become an important topic in electrical networks. HD techniques constitute alternative methods for the modelling and simulation of electrical networks with emphasis on the analysis of the power quality. HD simulations provide the steady state solution of an electrical network in a direct manner and power quality indices are readily available.

This chapter presents a HD model of an interconnected PV generation system. The topology of the interconnected PV generation system is the same as the one used in chapter 3 but the PV array and the grid are represented as Thévenin equivalents in HD. The proposed methodology is based on the set of first order ODE that represent the entire electrical system and converted into the HD. Also, switching functions (of the DC/DC and DC/AC converters) are represented in the HD as the Toeplitz-type matrices. This allows to obtain the steady state of the PV system via simple matrix/vector operations.

4.2 Electrical Variables in Harmonic Domain

4.2.1 Voltages and Currents

The HD uses the specific vector arrangement of the Fourier coefficients shown in (4.1) A HD signal will be hereafter represented by capital letters and instantaneous TD variables by lower case letters.

$$X = \begin{bmatrix} X_{-h} \\ \vdots \\ X_{-2} \\ X_{-1} \\ X_0 \\ X_1 \\ X_2 \\ \vdots \\ X_h \end{bmatrix} \tag{4.1}$$

In (4.1), h represents the maximum harmonic under study and the subscript "0" denotes the dc component.

Equation (4.1) shows that the DC component is located at the center of the vector, the terms above the DC component correspond to the Fourier coefficients with negative exponents in a descending order, the terms below the DC component are their flipped conjugates. Any current, voltage, or other electrical variable, can be expressed in the HD using the arrangement in (4.1).

In the case of a TD-sampled signal with unknown Fourier coefficients, FFT can be applied to obtain the harmonic coefficients in Section 2.6, taking care of the appropriate reordering of the obtained values, as dictated by (4.1).

4.2.2 HD Impedance/Admittance Relations of RLC Elements

The relation between voltage and current for the RLC elements in the HD are described next. Based on (4.1), consider the following generic definitions for the HD voltage and current vectors:

$$V = \begin{bmatrix} V_{-h} \\ \vdots \\ V_{-2} \\ V_{-1} \\ V_0 \\ V_1 \\ V_2 \\ \vdots \\ V_h \end{bmatrix}, \quad I = \begin{bmatrix} I_{-h} \\ \vdots \\ I_{-2} \\ I_{-1} \\ I_0 \\ I_1 \\ I_2 \\ \vdots \\ I_h \end{bmatrix} \tag{4.2}$$

Then, the TD relations for the RLC elements:

$$\mathrm{v_R(t) = Ri_R(t)}, \tag{4.3a}$$

$$\mathrm{v_L(t) = L\frac{di_L(t)}{dt}}, \tag{4.3b}$$

$$\mathrm{v_c(t) = \frac{1}{C}\int i_c(t)dt}, \tag{4.3c}$$

become in the HD:

$$V_R = RI_dI_R = Z_RI_R, \tag{4.4a}$$

$$V_L = LDI_L = Z_LI_L, \tag{4.4b}$$

$$V_C = \frac{1}{C}D^{-1}I_C = Z_cI_c, \tag{4.4c}$$

where the differentiation matrix D is defined as:

$$D = \begin{bmatrix} -jhw_0 & 0 & 0 & 0 & 0 & 0 & 0 & 0 & 0 \\ 0 & \ddots & 0 & 0 & 0 & 0 & 0 & 0 & 0 \\ 0 & 0 & -j2w_0 & 0 & 0 & 0 & 0 & 0 & 0 \\ 0 & 0 & 0 & -jw_0 & 0 & 0 & 0 & 0 & 0 \\ 0 & 0 & 0 & 0 & 0 & 0 & 0 & 0 & 0 \\ 0 & 0 & 0 & 0 & 0 & jw_0 & 0 & 0 & 0 \\ 0 & 0 & 0 & 0 & 0 & 0 & j2w_0 & 0 & 0 \\ 0 & 0 & 0 & 0 & 0 & 0 & 0 & \ddots & 0 \\ 0 & 0 & 0 & 0 & 0 & 0 & 0 & 0 & jhw_0 \end{bmatrix} \tag{4.5}$$

and I_d represents an identity matrix of dimensions $2h + 1$.

Similarly, the corresponding admittance relations are given by:

$$I_R = \frac{1}{R} I_d V_R = Y_R V_R, \tag{4.6a}$$

$$I_L = \frac{1}{L} D^{-1} V_L = Y_L V_L, \tag{4.6b}$$

$$I_C = CDV_C = Y_c V_c, \tag{4.6c}$$

Thus, the HD inclusion of RLC elements in a general network is performed by a set of algebraic equations, as given by (4.4) or (4.6).

4.2.3 Convolutions

For nonlinear elements, e.g., a nonlinear reactor, a voltage-current solution can be established in the HD via FD convolutions. As an illustrative example, consider the TD nonlinear relation given by (4.7), where $\mathrm{x(t)}$ and $\mathrm{y(t)}$ can represent electrical variables:

$$\mathrm{y(t)} = \mathrm{x(t)} + 0.1\mathrm{x(t)}^2 \tag{4.7}$$

In the HD, (4.7) becomes:

$$Y = X + 0.1(X \otimes X) \tag{4.8}$$

where $X \otimes X$ represents a FD convolution given in the HD as a product of a Toeplitz-type matrix with the harmonic content of X as elements and the HD vector X as follows:

$$X \otimes X = \begin{bmatrix} X_0 & X_{-1} & \cdots & X_{-h} & & & \\ X_1 & X_0 & X_{-1} & \cdots & \ddots & & \\ \vdots & X_1 & X_0 & \ddots & \cdots & \ddots & \\ X_h & \vdots & \ddots & \ddots & \ddots & \cdots & X_{-h} \\ & \ddots & \vdots & \ddots & X_0 & X_{-1} & \vdots \\ & & \ddots & \vdots & X_1 & X_0 & X_{-1} \\ & & & X_h & \cdots & X_1 & X_0 \end{bmatrix} \tag{4.9}$$

Periodically switched devices can also be represented in the HD via FD convolutions using switching functions. Consider the circuit of Fig. 4.1, which consists of an ideal switch and a resistive load.

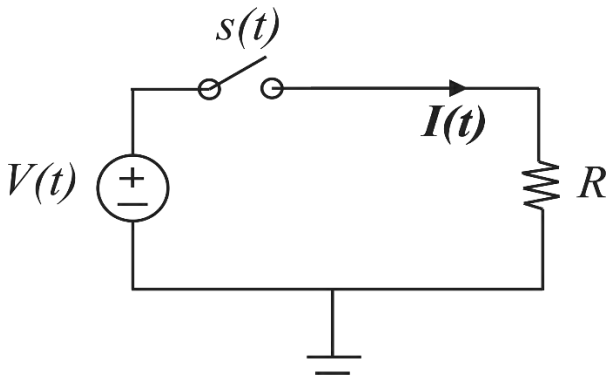

Fig. 4.1 Periodic switched load.

In the TD, the expression for the load current is:

$$\mathrm{i(t)} = \frac{1}{\mathrm{R}}\mathrm{s(t)v(t)} \tag{4.10}$$

where $\mathrm{s(t)}$ take values of one (switch on) or zero (switch off) along the time. If the switching scheme is periodic, $\mathrm{s(t)}$ can be represented by Fourier series. Therefore, the TD product of $\mathrm{s(t)}$ with $\mathrm{v(t)}$ becomes a convolution in the HD, and (4.10) can be written in the HD as:

$$I = \frac{1}{R} S \otimes V \tag{4.11}$$

It should be mentioned that a convolution generates a truncation error. This error becomes smaller as the number of terms taken from the Fourier series is increased.

4.3 Power Factor and Total Harmonic Distortion

Non-linear loads and electronic equipment generate harmonics which increase the root mean square (RMS) current, and therefore increase the apparent power consumption and decrease power factor. Based on this reasoning, some definitions for power quality are needed [Acha and Madrigal 2001], [Alexander and Sadiku 2006].

The RMS value of a signal in the HD is:

$$X_{RMS} = \sqrt{\sum_{m=-\infty}^{\infty} |X_m|^2} \tag{4.12}$$

Using the RMS value, as in (4.12), for voltage and current, the apparent power becomes:

$$S = \sqrt{\sum_{m=-\infty}^{\infty} \sum_{n=-\infty}^{\infty} |V_m|^2 |I_n|^2} \tag{4.13}$$

The apparent power of (4.13) can be represented as the sum of three orthogonal components as:

$$S = \sqrt{P^2 + Q_H^2 + D_H^2} \tag{4.14}$$

where P represents the active power (W), Q_H is the interaction of harmonic components of same frequencies (VAR), and D_H represents the interaction of harmonics of different frequencies. D_H is called Volts-Amperes-Distortion (VAD) [De la Rosa 2005].

The active power in a circuit with harmonic distortion is calculated with [Acha and Madrigal 2001]:

$$P = \sum_{m=-\infty}^{\infty} |V_m||I_{-m}| \tag{4.15}$$

then, power factor is given by:

$$PF = \frac{P}{S} \tag{4.16}$$

The THD of an electrical signal, either voltage or current, is:

$$THD_X = \frac{\sqrt{\sum_{m=2}^{\infty} |X_m|^2}}{|X_1|} \times 100\% \tag{4.17}$$

where X stands for V or I. The standards IEEE-519 and IEC-61000 define limits for harmonic distortion [De la Rosa 2015]. According to IEEE-519, the maximum admitted levels for THD in voltage for systems of up to 69 kV is 5% and any individual harmonic should not exceed 3%. For THD of currents, the maximum admitted level is calculated as a function of the short-circuit current at the PCC and the average of the maximum demand current based on periodic measurements [De la Rosa 2005].

4.4 State-Space Representation of the Grid-Connected PV Generation System.

Based on Fig. 3.10, the equivalent circuit of a single-phase grid-connected PV generation system is presented in Fig. 4.2. The PV array and the grid have been replaced by the corresponding Thévenin equivalents. The state-space representation of grid-connected PV generation system is composed by six ODEs.

$$\dot{x} = \begin{bmatrix} -\frac{1}{C_{pv}R_{pv}} & -\frac{1}{C_{pv}} & 0 & 0 & 0 & 0 \\ \frac{1}{L} & 0 & -\frac{s_2}{L} & 0 & 0 & 0 \\ 0 & \frac{s_2}{C} & 0 & -\frac{s_i}{C} & 0 & 0 \\ 0 & 0 & \frac{s_i}{L_{fc}} & -\frac{(R_{fc}+R_d)}{L_{fc}} & -\frac{1}{L_{fc}} & \frac{R_d}{L_{fc}} \\ 0 & 0 & 0 & \frac{1}{C_f} & 0 & -\frac{1}{C_f} \\ 0 & 0 & 0 & \frac{R_d}{(L_{fg}+L_g)} & \frac{1}{(L_{fg}+L_g)} & -\frac{(R_d+R_{fg}+R_g)}{L_{fg}+L_g} \end{bmatrix} \begin{bmatrix} v_{pv} \\ i_L \\ v_c \\ i_{fc} \\ v_{cf} \\ i_{pcc} \end{bmatrix} + \begin{bmatrix} \frac{1}{C_{pc}R_{pv}} & 0 \\ 0 & 0 \\ 0 & 0 \\ 0 & 0 \\ 0 & 0 \\ -\frac{1}{(L_{fg}+L_g)} & 0 \end{bmatrix} \begin{bmatrix} V_{th} \\ v_{AC} \end{bmatrix} \quad (4.18)$$

where:

$$s_i = s_{a1} - s_{b2} \quad (4.19)$$

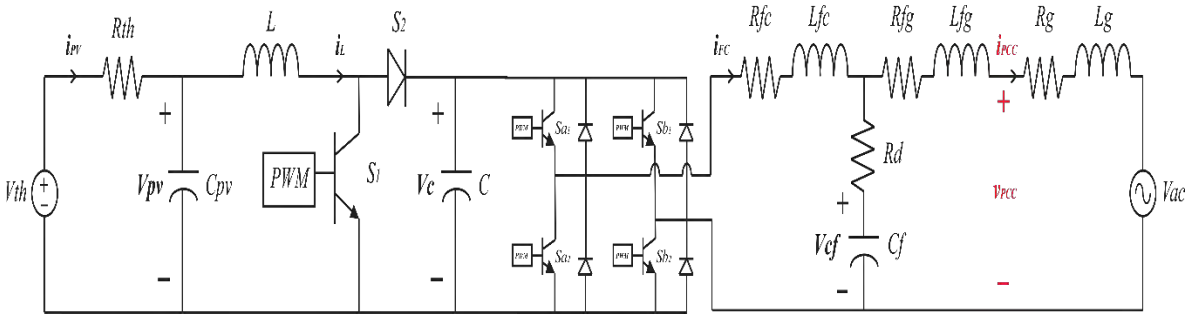

Fig. 4.2 Equivalent circuit of the grid-connected PV generation system.

The switching functions s_{a1} and s_{b2} are obtained with the PWM scheme of the VSI presented in Section 3.2.3, while s_2 is obtained based on the duty ratio of the BC. In (4.18), s_2 can take values of 1 or 0, while s_i can take values of 1, 0 or -1 along the time. Equation (3.23) or (4.18) represent the TD model of the single-phase grid-connected PV generation system. The transformation of the TD model to the HD is described next.

4.5 General Harmonic Domain Solution Scheme

Based on the HD theory of this chapter, the set of ODEs is given by (3.23) or (4.18) is converted into the HD resulting in:

$$D_d X = AX + BU \tag{4.20}$$

where:

$$D_d = \begin{bmatrix} D & & & & & & \\ & D & & & & & \\ & & D & & & & \\ & & & D & & & \\ & & & & D & & \\ & & & & & D & \end{bmatrix} \tag{4.21}$$

$$X = \begin{bmatrix} V_{pv} \\ I_L \\ V_c \\ I_{fc} \\ V_{cf} \\ I_{pcc} \end{bmatrix} \tag{4.22}$$

$$A=\begin{bmatrix} -\frac{1}{C_{pv}R_{pv}}I_d & -\frac{1}{C_{pv}}I_d & 0 & 0 & 0 & 0 \\ \frac{1}{L}I_d & 0 & -\frac{1}{L}S_2 & 0 & 0 & 0 \\ 0 & \frac{1}{C}S_2 & 0 & -\frac{1}{C}S_i & 0 & 0 \\ 0 & 0 & \frac{1}{L_{fc}}S_i & -\frac{(R_{fc}+R_d)}{L_{fc}}I_d & -\frac{1}{L_{fc}}I_d & \frac{R_d}{L_{fc}}I_d \\ 0 & 0 & 0 & \frac{1}{C_f}I_d & 0 & -\frac{1}{C_f}I_d \\ 0 & 0 & 0 & \frac{R_d}{(L_{fg}+L_g)}I_d & \frac{1}{(L_{fg}+L_g)}I_d & -\frac{(R_d+R_{fg}+R_g)}{L_{fg}+L_g}I_d \end{bmatrix} \tag{4.23}$$

$$BU=\begin{bmatrix} \frac{1}{C_{pc}R_{pv}} \\ 0 \\ 0 \\ 0 \\ 0 \\ -\frac{1}{(L_{fg}+L_g)} \end{bmatrix} \tag{4.24}$$

In (4.21) the differentiation matrix D has been arranged in block-diagonal form to account for the six HD variables, as given by (4.22). Also, the switching functions s_i and s_2 are represented in the HD as the Toeplitz-type matrices S_i and S_2, respectively, and introduced in matrix A given by (4.23). Please notice that in (4.23) I_d represents an identity matrix of appropriate dimensions.

The HD solution of (4.20) or alternatively the steady-state solution of the PV system for a given operating point, is given by:

$$X = (D_d - A)^{-1}BU \tag{4.25}$$

It is noted that i_{pv} is not a state variable and thus not a solution given by (4.25); however, it can be calculated with:

$$I_{pv} = \frac{1}{R_{pv}} V_{DC} - \frac{1}{R_{pv}} V_{pv} \tag{4.26}$$

Any HD solution vector, e.g., V_{pv} can be extracted from the X in (4.25) and transformed to the TD for waveform visualization purposes.

The flow chart of the solution method to obtain the periodic steady state of electrical networks with PV energy sources in HD is shown in Fig. 4.3. It is basically composed by five blocks. The first block reads the parameters of the electrical network and the PV generation system, the second block obtains the Thevenin equivalent circuit of the PV array and the power network, the third block is based on the circuit of Fig 4.2 to obtain the set of ODEs and convert it into the HD. Fourth block represents switching functions in the HD as the Toeplitz-type matrices and introduce them in matrix A. Finally, fifth block calculates the solution of the PV generation system for a given operating point. In other words, this block obtains the steady state of the entire electrical system via simple matrix/vector operations.

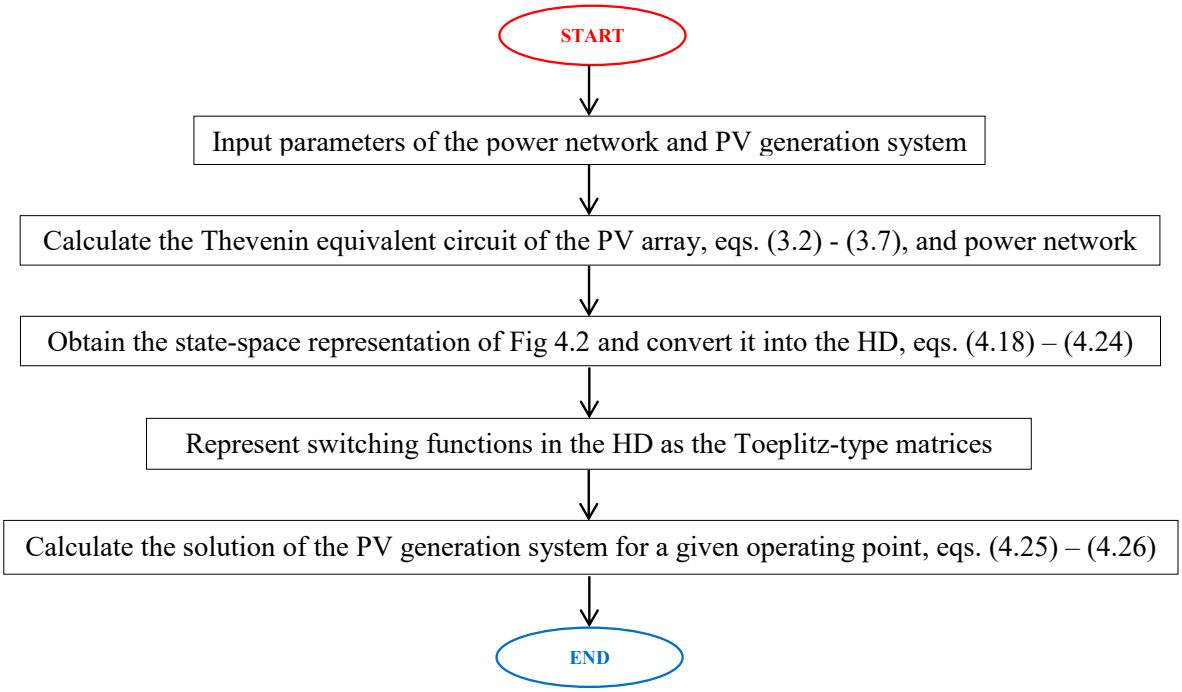

Fig. 4.3 Flowchart of the HD method.

4.6 Test Case of PV system in HD

The HD model of the single-phase grid-connected PV generation system (Fig. 4.2) and the solution scheme (Section 4.5) presented in this Chapter are adopted for the simulation results of this case. The dynamic operation of the system is represented by six ODEs. The voltage at the capacitors and the currents in the inductors where chosen as state variables. Data for the entire electrical network are contained in Table 4.1. The resultant variables of the PV array are obtained via the procedure described in section 3.2.1 and presented in Table 3.2.

Table 4.1 Data for grid-tied PV generation system.

PV array at STC		
N_S	17	Number of modules connected in series
N_P	2	Number of modules connected in parallel
V_{oc}	21.47 V	Open-circuit voltage per module
I_{sc}	7.6 A	Short-circuit current per module
V_{mpp}	17.1 V	Voltage at MPP per module
I_{mpp}	7.1 A	Current at MPP per module
P_{max}	121.41 W	Maximum power per module
n_S	28	Number of cells connected in series per module
k_i	0.00502 A/°C	Temperature correction factor for current
k_v	-0.08 V/°C	Temperature correction factor for voltage
a	1.3	Ideality factor of diode
DC/DC Converter		
C_{pv}	5500 μF	Capacitance
L	9 mH	Inductance
C	2200 µF	Capacitance
F_s	10 kHz	Switching Frequency
DC/AC Converter		
F_{SW}	25 kHz	Switching Frequency
m_a	0.9	Modulation index
Filter		
R_{fc}	1 mΩ	Resistance

L_{fc}	0.3 mH	Inductance
R_{fg}	1 mΩ	Resistance
L_{fg}	0.15 mH	Inductance
R_d	2 Ω	Resistance
C_f	2.2 μF	Capacitance
Network equivalent		
V_{AC}	215 V	Voltage (RMS)
R_g	1.84 Ω	Resistance
L_g	3.5 mH	Inductance

Figs. 4.4 - 4.7 present the resultant TD waveforms and the corresponding harmonic content of the voltage at the PV array terminals (v_{pv}), the current across the BC inductor (i_L), and the voltage and current at the PCC (v_{pcc} and i_{pcc}), respectively. It is mentioned that, to obtain the TD waveforms presented in this chapter, (4.25) is evaluated with a sampling time-step or 0.1 μs.

The results of Figs. 4.4 – 4.7 have been obtained by using 50 and 220 harmonics in the HD model of the PV system. Please notice that higher order produced by power electronics components are not expected to appear beyond the twentieth harmonic. This is due to the filter operation. Thus, there is usually no need to use more than 50 harmonics in the HD simulation and to obtain the TD waveforms, i.e., using fewer harmonics represents an obvious saving in computational resources.

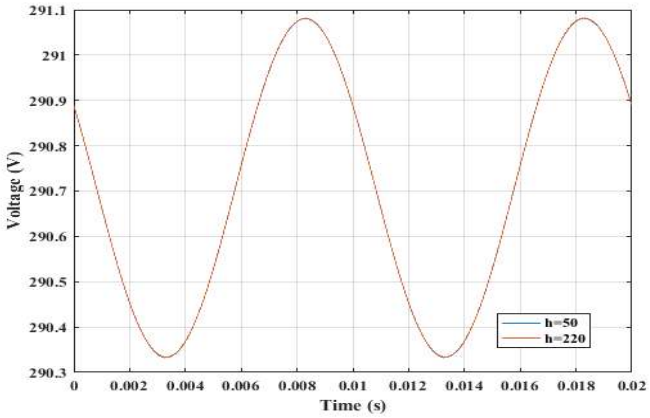

(a)

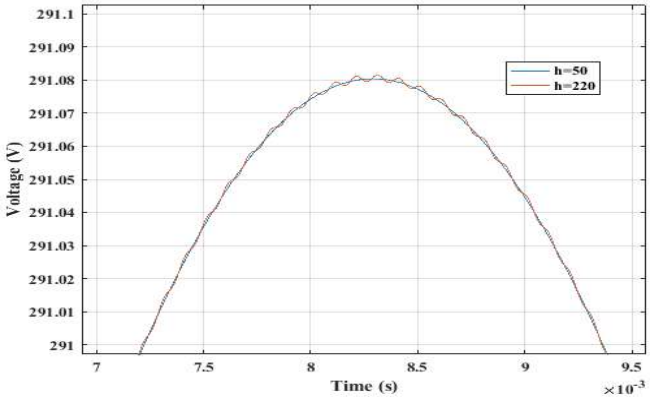

(b)

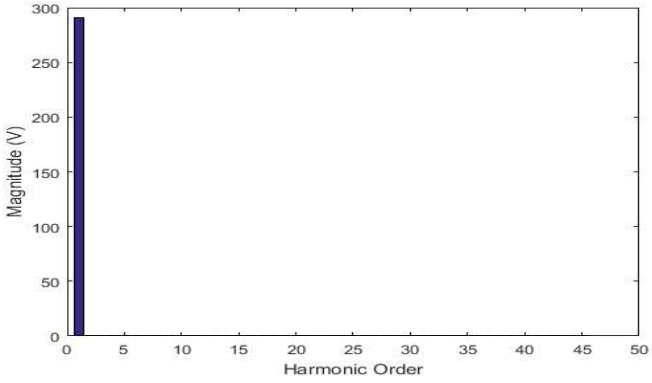

(c)

Fig. 4.4 (a) v_{pv}, (b) zoom-in of v_{pv}, and (c) harmonic content of v_{pv}.

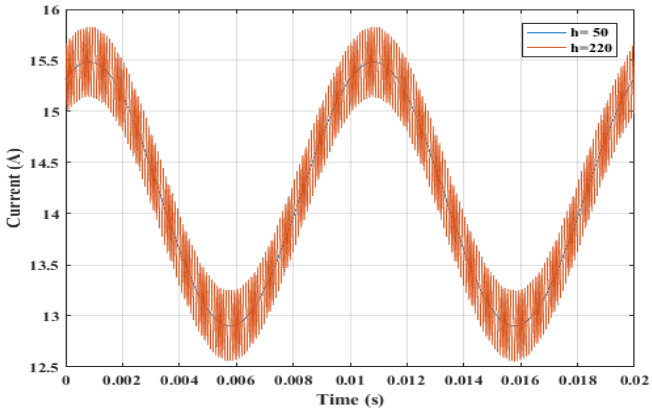

(a)

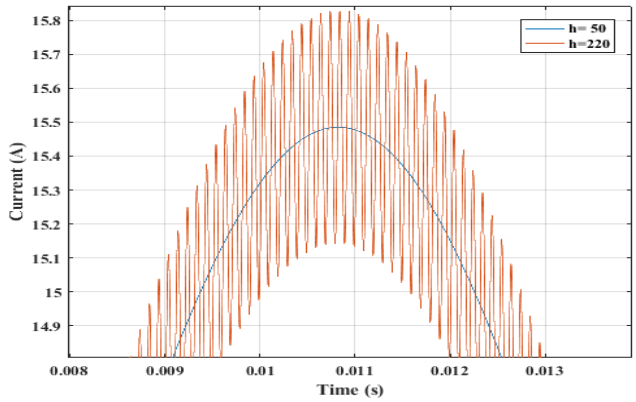

(b)

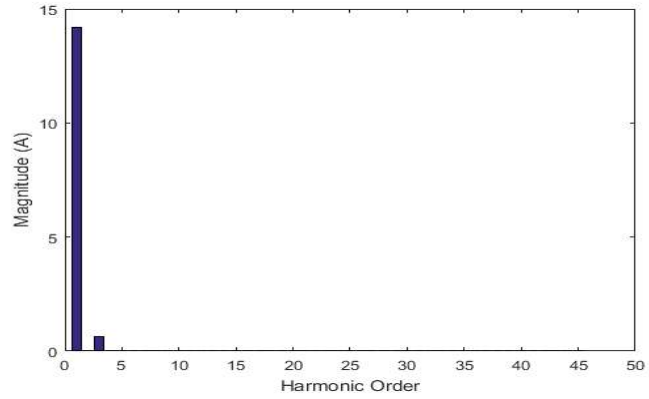

(c)

Fig. 4.5 (a) i_L, (b) zoom-in of i_L, and (c) harmonic content of i_L.

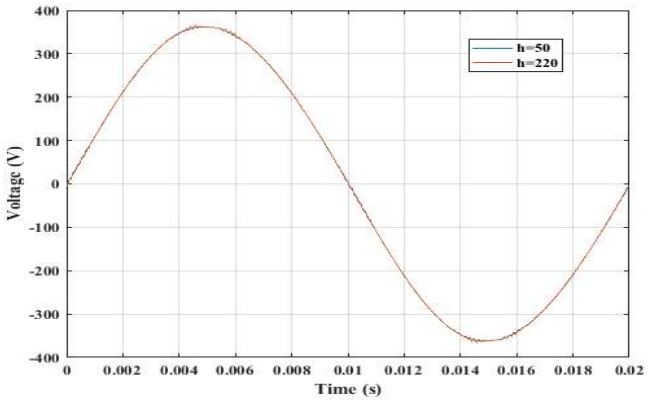

(a)

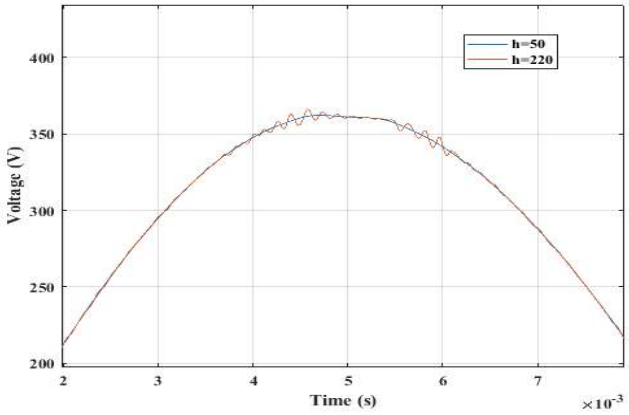

(b)

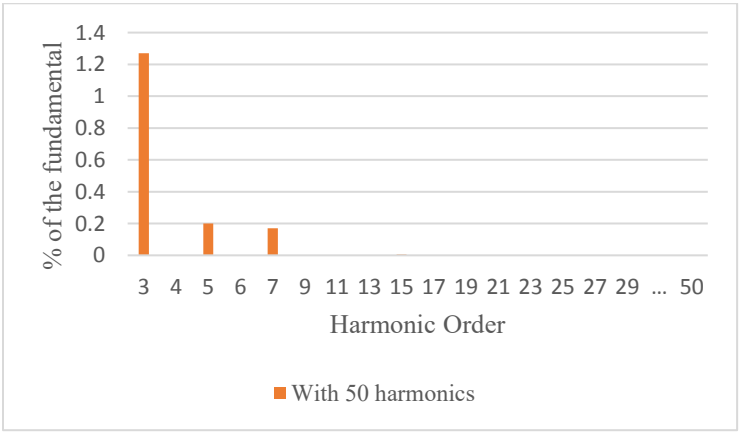

(c)

Fig. 4.6 (a) v_{pcc}, (b) zoom-in of v_{pcc}, and (c) harmonic content of v_{pcc}.

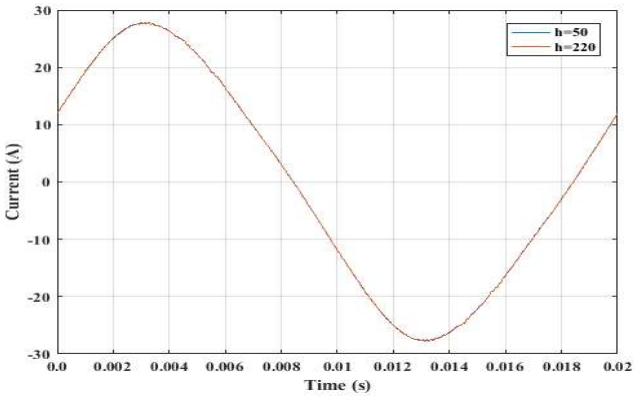

(a)

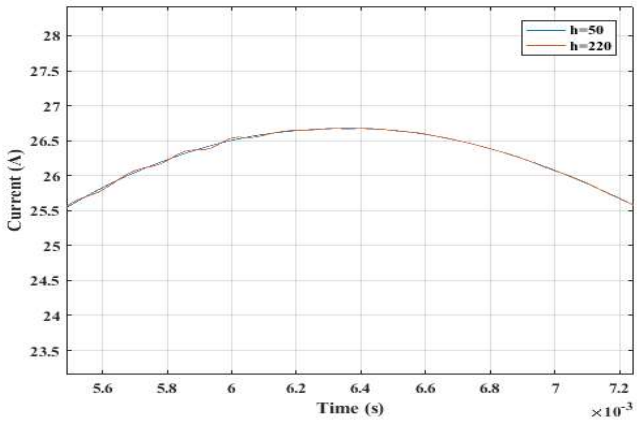

(b)

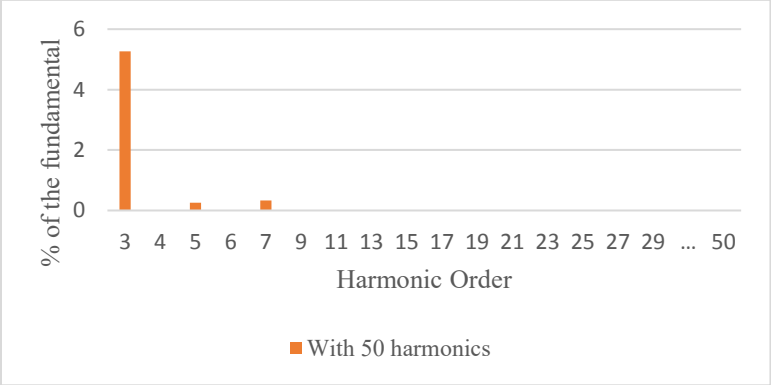

(c)

Fig. 4.7 (a) i_{pcc}, (b) zoom-in of i_{pcc}, and (c) harmonic content of i_{pcc}.

Fig. 4.8 shows a comparison between the voltage at the PV array terminals with the TD and the HD method. It can be observed that the calculated voltage using the HD model for 50 harmonics agrees well with the TD waveform, which means that there is a close agreement between both responses. However, the best way to compare this two current waveforms is by means of their harmonic spectra. This is done in Fig. 4.9, again a close agreement is shown.

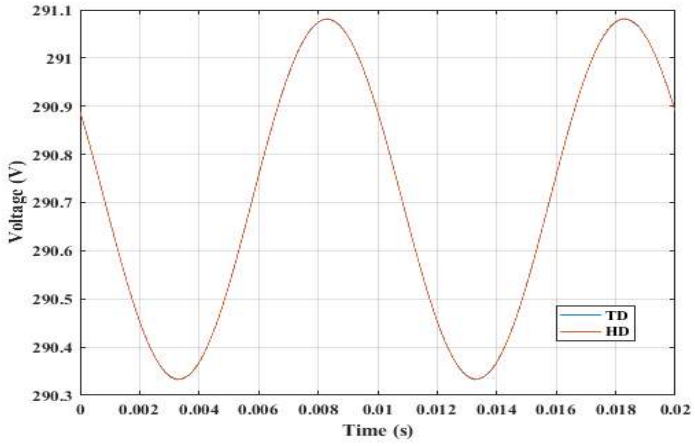

Fig. 4.8 Comparison between TD and HD of v_{pv}.

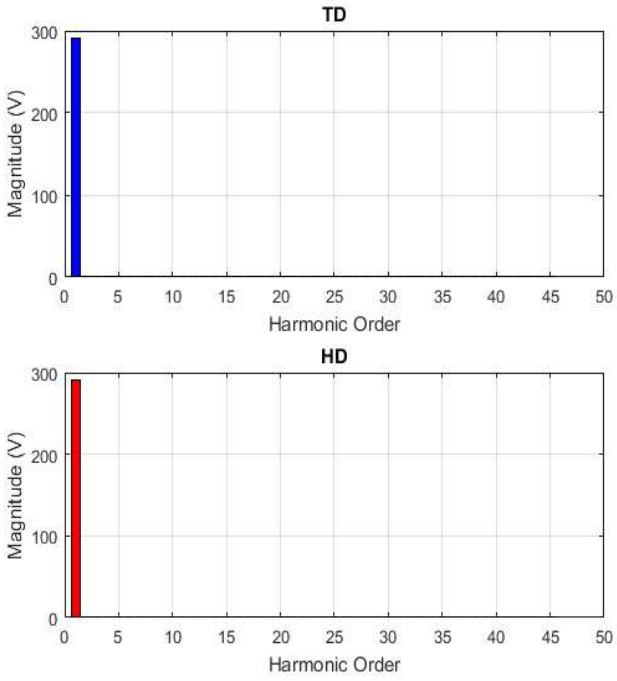

Fig. 4.9 Harmonic spectra of TD and HD of v_{pv}.

Table 4.2 shows the converged values of d and of the DC components (averages) of voltage and current at the PV array terminals using 220 harmonics. Table 4.2 concludes that the obtained values agree with the MPP as given in Table 3.2. Also the THD and powers at the PCC are shown in Table 4.2.

Table 4.2 Simulation results of HD case.

PV array		
V_{pv0}	290.7	DC component of voltage at PV terminals
I_{pv0}	14.20	DC component of current at PV terminals
Boost converter		
d	0.277	Duty Ratio
Point of common coupling		
THD in v_{pcc}	1.19 %	Total harmonic distortion
THD in i_{pcc}	5.29 %	Total harmonic distortion
S	4.7755 kVA	Apparent power
P	4.1330 kW	Active power
PF	0.8654	Power factor

4.7 Harmonic Propagation Method

The steady state solution of a linear circuit operating under non-sinusoidal conditions may be carried out using phasor analysis, but the circuit needs to be solved at each frequency of interest [Acha and Madrigal 2001]. The inductors and capacitors have linear frequency dependence, whereas the resistor may be assumed to remain constant. With these three passive elements and the sources represented by their harmonic content, a linear circuit analysis can be carried out.

In general, a linear circuit operating under non-sinusoidal conditions is well represented by the following linear system of equations:

$$\begin{bmatrix} I_h^1 \\ I_h^2 \\ \vdots \\ I_h^j \\ \vdots \\ I_h^N \end{bmatrix} = \begin{bmatrix} Y_h^{1,1} & Y_h^{1,2} & \cdots & Y_h^{1,j} & \cdots & Y_h^{1,N} \\ Y_h^{2,1} & Y_h^{2,2} & \cdots & Y_h^{2,j} & \cdots & Y_h^{2,N} \\ \vdots & \vdots & \ddots & \vdots & \ddots & \vdots \\ Y_h^{j,1} & Y_h^{j,2} & \cdots & Y_h^{j,j} & \cdots & Y_h^{j,N} \\ \vdots & \vdots & \ddots & \vdots & \ddots & \vdots \\ Y_h^{N,1} & Y_h^{N,2} & \cdots & Y_h^{N,j} & \cdots & Y_h^{N,N} \end{bmatrix} \begin{bmatrix} V_h^1 \\ V_h^2 \\ \vdots \\ V_h^j \\ \vdots \\ V_h^N \end{bmatrix} \tag{4.27}$$

where the current I_h^j is the phasor current at frequency h injected at node j, $Y_h^{i,j}$ is the equivalent admittance at frequency h between nodes i and j, V_h^j is the phasor voltage at frequency h at node j, and N is the number of nodes of the electric network.

Equation (4.27) in compact form is given by

$$I_h = Y_h V_h \tag{4.28}$$

where I_h is the harmonic current injection vector, Y_h is the harmonic equivalent admittance matrix, and V_h is the harmonic voltage vector. The system is solved at each frequency of interest as

$$V_h = Y_h^{-1} I_h \tag{4.29}$$

The inverse of the admittance matrix Y_h gives the impedance matrix Z_h,

$$Z_h = \begin{bmatrix} Z_h^{1,1} & Z_h^{1,2} & \cdots & Z_h^{1,j} & \cdots & Z_h^{1,N} \\ Z_h^{2,1} & Z_h^{2,2} & \cdots & Z_h^{2,j} & \cdots & Z_h^{2,N} \\ \vdots & \vdots & \ddots & \vdots & \ddots & \vdots \\ Z_h^{j,1} & Z_h^{j,2} & \cdots & Z_h^{j,j} & \cdots & Z_h^{j,N} \\ \vdots & \vdots & \ddots & \vdots & \ddots & \vdots \\ Z_h^{N,1} & Z_h^{N,2} & \cdots & Z_h^{N,j} & \cdots & Z_h^{N,N} \end{bmatrix} \tag{4.30}$$

where the impedance $Z_h^{i,j}$ is known as the *driving point impedance* of node j at different frequencies.

4.8 Current Injection Method

The harmonic current injection method (CIM) is widely used to carry out harmonic propagation studies in power systems [Heydt 1991].

The salient features of the method are outlined below:

- Build Y_h of the power system including the contribution for all sources and loads. A different Y_h must be calculated for each harmonic h.
- Obtain I_h by extracting the term of the appropriate frequency from each nonlinear load.
- Use (4.29) to calculate V_h. Both magnitude and phase information are important. If a time domain solution required for each bus voltage, the calculated harmonics are superimposed.

4.9 LU Decomposition

Since (4.29) should be repetitively used, once for each harmonic. It is advisable to form Y_h with an algorithm being time and memory efficient. For instance, triangular factorization may be applied. The triangular factors of Y_h are found and the voltages are calculated by appropriately applying forward and backward substitution to Equations (4.31) to (4.33).

$$I_h = (L)(U)V_h \tag{4.31}$$

$$I_h = (L)(W) \tag{4.32}$$

$$W = (U)V_h \tag{4.33}$$

In the above equations, L and U are the lower left and upper right triangular factors of Y_h. The vector W is solved by forward substitution, and the vector V_h is subsequently calculated by backward substitution.

4.10 General Harmonic Propagation Solution Procedure

The algorithm for the harmonic propagation method in the power network combines a conventional power flow study with the CIM and LU decomposition. Fig. 4.10 slows the flowchart for the harmonic propagation method. It is basically composed by three blocks, i.e., the data block that reads the parameters of the power system, the power flow block that performs a conventional power flow study and the harmonic voltage block that determines the harmonic propagation through the system. Some parts of the algorithm are executed sequentially and some parts in parallel. The system data block is programmed sequentially. Then two tasks are simultaneously run. Each task is performed by one thread in the CPU (Open MP). One of the threads (thread 1) performs the power flow study meanwhile the other thread (thread 0) copy the system data from the CPU to the GPU.

These two tasks are executed in parallel and have different computation time, so they have to be synchronized. To synchronize this part of the algorithm a flag is used. Initially flag = 0 and changes to flag = 1 when the power flow study concludes. If the power flow study has no finished yet, thread 0 will have to wait until thread 1 finishes its process. The last part of the algorithm is executed in the GPU (CUDA).

For each harmonic, it is necessary to obtain the equivalent admittance matrix, the CIM, and solve for the harmonic voltage vector. Superposition effects are accounted to obtain the final result.

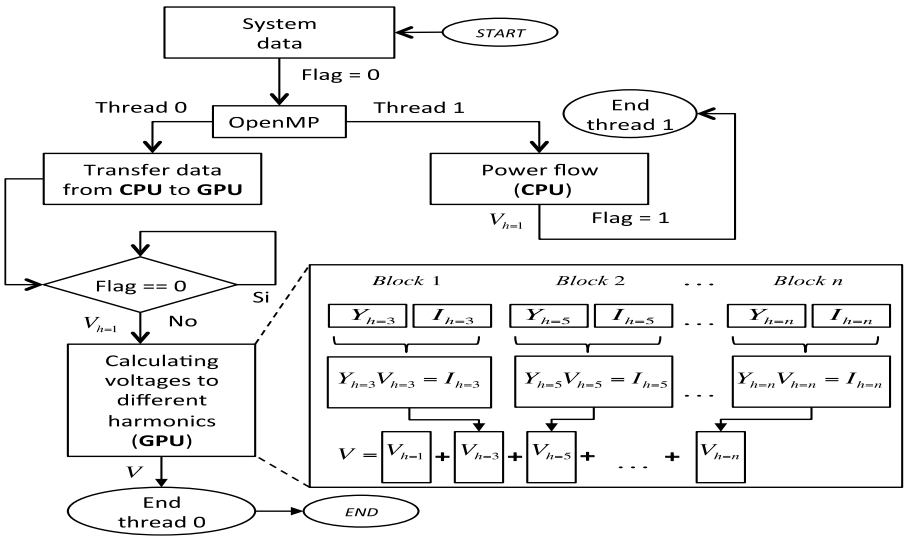

Fig. 4.10 Algorithm of the proposed method

The following steps summarize the complete method.

- Find the steady state solution given by a conventional power flow study.
- With the resultant voltages at fundamental frequency, compute the passive equivalent circuit.
- Obtain the equivalent admittance matrix seen from node where the non-linear load is connected.
- Solve (4.29) for each frequency of interest to get the final result by superposition of effects.

4.11 Harmonic Propagation in FD

A case study for the harmonic propagation in the power network using the methodology described in Section 4.7 is presented next. The solution algorithm of Section 4.10 was developed in the FD framework. For the purposes of the simulation, it is sufficient for harmonic analysis to account for the first 50 harmonics.

The test system of Fig. 4.11 has been used to illustrate the performance of the implemented method described in Section 4.7. It corresponds to a modified IEEE-14 bus test system. The electric power system includes three static VAR compensators (SVCs) connected in three different buses.

The maximum magnitudes of harmonic content injected by the SVCs are given in Table 4.3. The SVCs are considered to be delta connected, hence no zero sequence harmonic current is injected into system. In Table 4.3, the harmonic currents are given as percentage of the fundamental component. The fundamental power flow solution is given in Table 4.4.

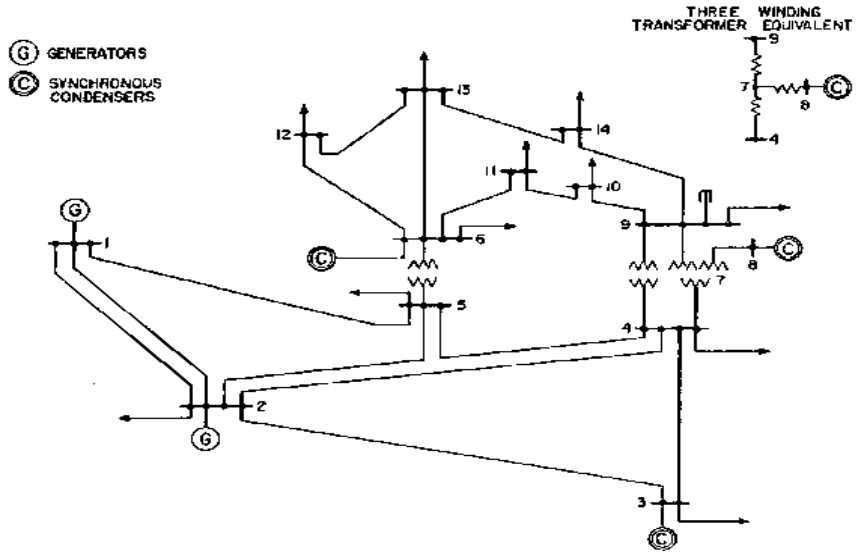

Fig. 4.11 IEEE-14 bus test system.

Table 4.3 Maximum amplitude of harmonic currents in SVC.

Harmonic	***% of fundamental***
5	5.05
7	2.59
11	1.05
13	0.75
17	0.44
19	0.35
23	0.24
25	0.20

Table 4.4 Fundamental frequency power flow (p.u.).

Node	$\lvert V \rvert$	θ	P_G	Q_G	P_D	Q_D
1	1.060	0	2.385	0	0	0
2	1.045	-5.109	0.400	0.122	0.217	0.127
3	1.010	-12.91	0	-0.182	0.942	0.190
4	1.024	-10.72	0	0	0.478	-0.039
5	1.023	-9.079	0	0	0.076	0.016
6	1.070	-14.53	0	-1.250	0.112	0.075
7	1.083	-14.03	0	0	0	0
8	1.090	-14.03	0	0.037	0	0
9	1.100	-15.68	0	0	0.295	0.166
10	1.087	-15.77	0	0	0.090	0.058
11	1.075	-15.32	0	0	0.035	0.018
12	1.155	-18.07	0	0	0.061	0.016
13	1.136	-17.53	0	0	0.135	0.058
14	1.170	-19.08	0	0	0.149	0.050

The system is solved for each frequency of interest with (4.29), where I_h have values different from zero only in entries where the nonlinear loads are connected. Table 4.5 shows the harmonic voltages in percentage of the fundamental.

Table 4.5 Harmonic voltage in the network.

V \ h	***5%***	***7%***	***11%***	***13%***	***17%***	***THD***
$\lvert V_{10} \rvert$	0.5548	0.6397	0.1646	0.0727	0.0238	0.8662
θ_{10}	129.60	104.52	-10.29	-19.272	-23.88	
$\lvert V_{11} \rvert$	0.2875	0.3267	0.0806	0.0346	0.0105	0.4441
θ_{11}	128.89	103.72	-11.29	-20.38	-25.22	
$\lvert V_{12} \rvert$	1.1192	0.7802	0.4406	0.3717	0.2815	1.5527
θ_{12}	149.58	148.30	153.31	154.19	155.32	
$\lvert V_{13} \rvert$	0.9679	0.6763	0.3441	0.2946	0.2244	1.3182
θ_{13}	147.67	143.67	151.85	153.07	154.29	
$\lvert V_{14} \rvert$	1.5306	1.1408	0.3504	0.3292	0.2644	2.0175
θ_{14}	141.39	129.81	144.64	149.31	151.55	

To show the impact that the nonlinear load has on these type of studies, Fig. 4.12 shows the distorted voltage waveform obtain at bus 14.

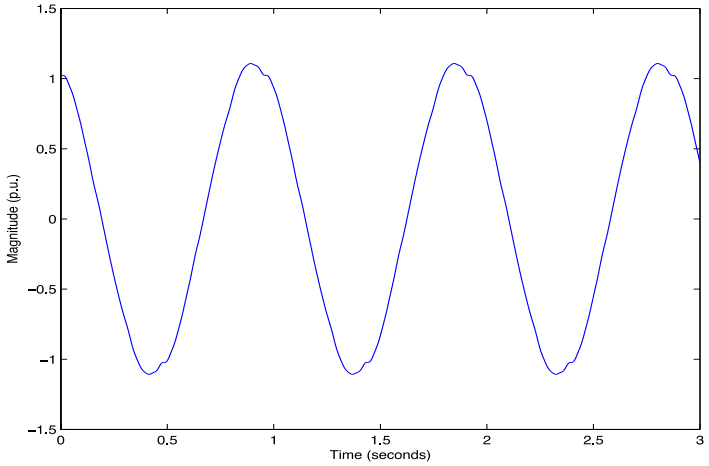

Fig. 4.12 Distorted voltage waveform at bus 14.

The parallel code has been applied to larger systems to show the relevance of the harmonic CIM processed in parallel. The IEEE-57, 118 and 300 test bus system have been solved. Table 4.6 shows the results obtained by the sequential and the parallelized algorithm. The first column shows the bus number, the second the time for data reading of power system, and the third is the time consumed by the power flow study. Columns fourth and fifth show the computation time of the CIM processed in parallel (PCI) and sequential (SCI), respectively. Columns sixth and seventh show the processing time for the complete parallel (TPCI) and sequential (TSCI) code, respectively. The last two columns show the speed-up of the complete algorithm and the speed-up of the CIM respectively.

Table 4.6 CPU time in larger systems FD.

IEEE system	***Data***	***Power Flow***	***PCI***	***SCI***	***TPCI***	***TSCI***	***Speedup SCI/PCI***
57	0	21	46	51	67	72	1.11
118	1	56	52	361	109	418	6.94
300	2	1250	592	7667	1844	8919	12.95

The comparison of the fourth column to the fifth shows the importance of using parallel processing based on GPUs for the CIM. The best speed-up is 12.95 times for the IEEE-300 bus test system and 4.84 times for the complete algorithm. For the case of the IEEE-118 bus test system the results were 6.94 and 3.83, respectively, and for the case of the IEEE-57 bus test system were 1.11 and 1.07, respectively. It is clear that the speed-up significantly increases with the size of the power network. The speed-up can be improved if the entire algorithm and not just the CIM are solved by using parallel processing.

4.12 Conclusions

The HD basic theory has been reviewed. The HD representation of nonlinear and switched-elements has been presented in terms of frequency domain convolutions. This representation allows to readily handle such elements via algebraic frequency domain operations. Furthermore, some power quality indices for nonsinusoidal conditions have been presented.

The HD model of a grid-connected PV generation system has been presented. A major characteristic of the proposed model is that the periodic steady-state can be obtained in a direct way via HD matrix/vector operations.

On the other hand, the proposed HD model of the single-phase grid-connected PV generation system has been also evaluated for STC. A major result is that the proposed model can include any number of harmonics depending on the desired TD resolution. Using fewer samples represents an obvious saving in computational resources. Finally, power quality indices are readily available from the HD solution variables.

A close agreement between the TD and HD methodologies for the assessment of the dynamic and the periodic steady state operation of microgrids with PV generation systems is shown. As evidence of it, the THD calculated for both cases is the same.

The application of parallel GPU-computing in harmonic propagation studies in FD for large electrical networks has been very effective and accurate.

Chapter 5

Conclusions

5.1 Conclusions

An efficient and accurate TD methodology to evaluate the dynamic operation and harmonic distortion of a single-phase grid-connected PV generation system has been proposed. The method combines the advantages of the ND method and CSI technique. The introduction of CSI significantly enhances the efficiently of the ND method for the computation of the periodic steady state solution. Besides, the algorithm with CSI accurately reproduces the steady state waveform of the ND method using a much larger number of time steps. The proposed ND-CSI methodology has been validated against the solution obtained with the conventional BF solution and with the PSCAD/EMTDC simulator, respectively. A close agreement between the obtained responses has been achieved. For the reported case 3.7, the maximum error between responses was 0.02%. The computational effort to obtain the TD solution has been substantially reduced when compared against the BF approach, i.e., on average the ND-CSI with $\mathbf{\Phi}$ variable was 10 times faster than the conventional BF solution and 20 times faster with $\mathbf{\Phi}$ constant.

A HD model of a single-phase grid-connected PV generation system has been also proposed. The Norton equivalent of the PV array and the Thevenin equivalent of the power network have been introduced in the HD model of case 4.6. The obtained results have been validated against the response obtained with the TD method; a close agreement was achieved. The simulation results show that higher harmonics produced by power electronics do not appear at the PCC due to the filter presence; however, lower harmonics are present.

In this thesis, the power network has been assumed without harmonic distortion, yielding low values of THD at the PCC. In real cases, some harmonics from the power network can produce a higher harmonic distortion. A distorted power network can be readily accounted for in the proposed model.

It is important to mention that the TD and HD model of a single-phase grid-connected PV generation system used in this research is exactly the same. A close agreement between the periodic steady state solution obtained in TD and HD, respectively, was achieved.

A parallel processing technique based on GPUs for the analysis of harmonic propagation in electric networks using the CIM and LU Decomposition in the FD has been applied in case study 5.3. It is shown that for the explicit harmonics representation, the implementation on a GPU platform becomes an efficient computational resource to find the steady state solution since floating-point operations and repetitive calculations increase in proportion to the number of harmonics and size of the network; both related with the computer effort.

The algorithm processed in parallel was implemented on a Tesla C2075 GPU. It improves the efficiency from 1.11 to 12.95 times for the CIM and from 1.07 to 4.84 times in total simulation, as compared with a conventional algorithm processed in series.

Finally, a TD methodology for the analysis of harmonic propagation in electric networks using the ND and CSI methods has been proposed in case 5.4.

For the modified IEEE-14 bus test system, the ND-CSI was on average 7 times faster than the BF method and 5 times faster than the ND method. For the modified IEEE-30 bus test system, the ND-CSI was on average 8 times faster than the BF method and 6 times faster than the ND method.

5.2 Recommendations for future research work

From the state of research reported in this thesis, the author suggests to proceed in the following directions:

1. To extend the reported representation of PV systems to include three-phase power networks, working under balanced and unbalanced operation conditions.
2. To extend the analysis to the power networks with integration of other renewable energy sources, such as wind generators, diesel generators, bank of batteries, among others.

3. To extend the analysis to the dynamic and periodic steady state solution of larger scale conventional power networks as well as with the integration of renewable energy sources.
4. To extend the analysis to other power quality adverse effects, such as inter-harmonics, sags, swells, flicker, among others.
5. To introduce control techniques in the HD and TD for MPPT using voltage source converters.
6. To further potentiate the application of parallel processing for the efficient dynamic and periodic steady state analysis of power networks with integration of renewable energy sources.
7. To explore the application of real time simulation in the analysis.

References

[Acha *et al*. 1990]

E. Acha, A. Semlyen, and N. Rajakovic, "A Harmonic Domain Computational Package for Nonlinear Problems and its Application to Electric Arcs", *IEEE Transactions on Power Delivery*, vol. 5, no. 3, pp. 1390-1397, Jul. 1990.

[Acha *et al*. 1996]

E. Acha, J. J. Rico, S. Acha, and M. Madrigal, "Harmonic Domain Modelling of the Three-phase Thryristor-controlled Reactors by Means of Switching Vectors and Discrete Convolutions", *IEEE Transactions on Power Delivery*, vol. 11, no. 3, pp. 1678-1684, Jul. 1996.

[Acha and Madrigal 2001]

E. Acha, M. Madrigal, "Power Systems Harmonics, Computer Modelling and Analysis", John Wiley & Sons, Chichester, England, 2001.

[Alexander and Sadiku 2006]

C. K. Alexander and M.N. Sadiku, "Fundamental of electric circuits", 3rd ed., Mc Graw Hill, 2006.

[Arrillaga and Watson 2004]

J. Arrillaga, N. R. Watson, "Power Systems Harmonics", 2nd ed., John Wiley & Sons, Canterbury, New Zeland, 2004.

[Balagurusamy 1999]

E. Balagurusamy, "Numerical Methods", Mc Graw Hill, 1999.

[Bathrurst *et al*. 2000]

G. N. Bathrurst, B. C. Smith, N. R. Watson, and J. Arrillaga, "Modelling of HVDC Transmission Systems in the Harmonic Domain", *IEEE Transactions on Power Delivery*, vol. 14, no. 3, pp. 1075-1080, Jul. 2000.

[Bathrurst *et al*. 2001]

G. N. Bathrurst, N. R. Watson, and J. Arrillaga, "A Harmonic Domain Solution for Systems with Multiple High-Power AC/DC Converters", *Proc. Inst. Elect. Eng.*, vol. 148, no. 4, pp. 312-318, Jul. 1995.

[Burden *et al.* 2011]

R. L. Burden, D. J. Fires, A. M. Burden, "*Numerical Analysis*", 9th ed., CENGAGE Learning, 2011.

[Chang 2003]

G. W. Chang, "Characterizing Harmonic Currents Generated by Fluorescent Lamps in Harmonic Domain", *IEEE Transactions on Power Delivery*, vol. 18, no. 4, pp. 1583-1585, Oct. 2003.

[Chapman *et al.* 2008]

B. Chapman, G. Jost, and A. R. Van Der Pas, "Using OpenMP: Portable Shared Memory Parallel Programing", The MIT Press, London, England, 2008.

[Chapra and Canale 2010]

S. C. Chapra, R. P. Canale, "*Numerical Methods for Engineers*", 6th ed., Mc Graw-Hill, 2010.

[Chen *et al*. 2010]

L. R. Chen, C. S. Tsai, Y. L. Lin, and Y. S. Lai, "A Biological Swarm Chasing Algorithm for Tracking the PV Maximum Power Point", *IEEE Trans. Energy Convers.*, vol. 25, no. 2, pp. 484-493, Jun 2010.

[Cheney and Kincaid 2008]

W. Cheney, D Kincaid, "*Numerical Mathematics and Computing*", 6th ed., Brooks/Cole, Monterey, CA, 2008.

[Collins *et al*. 2006]

C. D. Collins, N. R. Watson, and A. Wood, "UPFC Modeling in the Harmonic Domain" *IEEE Transactions on Power Delivery*, vol. 21, no. 2, pp. 933-938, Apr. 2006.

[Cook 2013]

S. Cook,"CUDA programming: A Developers Guide to Parallel Computing Based on GPUs", Morgan Kaufmann, Massachusetts, USA, 2013.

[De la Rosa 2015]

F. C. De la Rosa, "Harmonics, Power Systems, and Smart Grids", CRC Taylor and Francis, 2nd edition, 2015.

[Dommel *et al*. 1986]

H. W. Dommel, A. Yan, and S. Wei, "Harmonics from Transformer Saturation", *IEEE Trans. Power Syst.*, vol. PWRD-1, no. 2, pp. 209-214, Apr. 1986.

[Eltawil and Zhao 2010]

M. A. Eltawil, Z. Zhao, "Grid-connected photovoltaic power systems: technical and potential problems-A review", *Renewable and sustainable Energy Reviews*, vol. 14, no.1, pp. 112-129, Jan 2010.

[EMPT-RV 2012]

EMPT-RV User´s Guide, Version 3.0, Develop by powersys, Quebec, Canada, Apr. 2012.

[Heydt 1991]

G. T. Heydt, "Electric Power Quality", Stars in a Circle Publications, May 1991.

[IEEE Std 519-1992]

IEEE Std 519-1992, IEEE Recommended Practices and Requirements for Harmonic Control in Electrical Power Systems, 1992.

[Jain and Agarwal 2008]

S. Jain and V. Agarwal, “An Integrated Hybrid Power Supply for Distributed Generation Applications Fed by Nonconventional Energy Sources”, *IEEE Trans. Energy Convers.*, vol. 23, no. 2, pp. 622-631, Jun 2008.

[Kalogirou 2013]

S. A. Kalogirou, “Solar Energy Engineering”, 2nd ed., Elsevier, 2013.

[Kim *et al.* 2009]

S. K. Kim, J. H. Jeon, C. H. Cho, E. S. Kim, J. B. Ahn, “Modeling and simulation of a grid connected PV generation system for electromagnetic transient analysis”, Solar Energy, vol. 83, no.5, pp. 664-678, May 2009.

[Kouro *et al*. 2015]

S. Kouro, J. I. Leon, D. Vinnikov, L. G. Franquelo, “Grid-Connected Photovoltaic Systems: An Overview of Recent Research and Emerging PV Converter Technology”, *IEEE Industrial Electronics Magazine*, vol. 9, no.1, pp. 47-61, March 2015.

[Lee and Wang 2008]

D. J. Lee and L. Wang, “Small-Signal Stability Analysis of an Autonomous Hybrid Renewable Energy Power Generation/Energy Storage System part I: Time-domain simulations”, *IEEE Trans. Energy Convers.*, vol. 23, no. 1, pp. 311-320, Mar 2008.

[Luo and Ye 2004]

F. L. Luo and H. Ye, *“Advanced DC/DC Converters”*, CRC Press, 2004.

[Magaña 2016]

E. Magaña Lemus, “Técnicas numericas y computacionales aplicadas a la solución en estado estacionario periódico de redes electricas”, Tesis de doctorado, U.M.S.N.H., Enero 2016.

[Martin Bucher 2016]

Martin Bucher, Solar Park Pocking Bavaria, Germany [Online]. Available: www.martin-butcher.de

[Masters 2004]

G. M. Masters, *"Renewable and efficient electric power systems"*, Wiley-Interscience, 2004.

[Medina *et al*. 1994]

A. Medina, J. Arrillaga, and J. F. Eggleston, "A synchronous machine model in the harmonic domain", in *Proc. IEEE Int. Conf. Elect. Mach.*, Manchester, U. K., pp. 647-651. 1994.

[Medina *et al.* 2013]

A. Medina, J. Segundo, P. Ribeiro, W. Xu, K. L. Lian, G. W. Chang, and N. R. Watson, "Harmonic Analysis in Frequency and Time Domain", *IEEE Transactions on Power Delivery*, vol. 28, no. 3, pp. 1813-1821, Aug. 2013.

[Medina and Arrillaga 1992]

A Medina and J. Arrillaga, "Generalized Modelling of Power Transformers in the Harmonic Domain", *IEEE Transactions on Power Delivery*, vol. 7, no. 3, pp. 1458-1465, Jul. 1992.

[Messenger and Ventre 2010]

R. A. Messenger and J. Ventre, *"Photovoltaic systems engineering"*, 3rd ed., CRC Press, 2010.

[Moller 1993]

H. J. Moller, *"Semiconductors for Solar Cells"*, Norwood, MA: Artech House, 1993.

[Morales 2014]

J. Morales Rodríguez, *"Modeling Single-Phase Grid-Tied Photovoltaic generation System en the Harmonic Domain",* PhD thesis, CINVESTAV Unidad Guadalajara, Guadalajara, Jalisco, México. 2014.

[Mohan *et al.* 2001]

N. Mohan, T. M. Undeland, W. P. Robbins, "*Power Electronics: Converters, Applications, and Design*", 3rd edition, John Wiley & Sons, 2001.

[Nvidia CUDA 2015]

Nvidia CUDA Compute Architecture, "Programming Guide", 2015.

[Nvidia Fermi 2011]

Nvidia Fermi Architecture, "Specification: Tesla C2075 GPU Computing system", 2011.

[Nvidia Kepler 2012].

Nvidia Kepler Architecture, "Specification: GeForce GTX 650 Computing system", 2012.

[OpenMP 2013]

OpenMP Application Program Interface, Version 4.0, July 2013.

[Otto and Denier 2005]

S. R. Otto and J. P. Denier, "An Introduction to Programming and Numerical Methods in Matlab", Springer, 2005.

[Patel 2006]

M. R. Patel, *"Wind and solar power systems: design, analysis and operations"*, 2nd ed., CRC Press, 2006.

[Parker and Chua 1989]

T. S. Parker, L.O. Chua, *"Practical Numerical Algorithms for Chaotic Systems"*, Springer-Verlag, 1989.

[Perera *et al*. 2012]

B. K. Perera, S. R. Pulikanti, P. Ciufo, and S. Perera, "Simulation Model of a Grid-Connected Single-Phase Photovoltaic System in PSCAD/EMTDC," *Proc. Of the IEEE Power System Technology* (POWERCON), 2012.

[Proakis and Manolakis 1996]

J. G. Proakis and D.G. Manolakis, "Digital Signal Processing, principles, algorithms and applications", 3rd ed., Prentice Hall, 1996.

[PSCAD 2005]

PSCAD User´s Guide, Version 4.2.0, Develop by HVDC Research Center Inc., Manitoba, Canada, Apr. 2005.

[PSIM 2016]

PSIM User´s Guide, Version 10.0, Develop by Powersim, Rockville, MD United States, Jan. 2016.

[Quinn 2004]

M. J. Quinn, "Parallel Programing in C with MPI and OpenMP", Mc Graw-Hill, 2004.

[Ramos 2007]

A Ramos-Paz, "Técnica para la generación automática de ecuaciones diferenciales no autónomas para representar el comportamiento dinámico se sistemas eléctricos no lineales incorporando herramientas avanzadas de computo", Tesis de doctorado, U.M.S.N.H., Enero 2007.

[Rashid 2011]

M. H. Rashid, "*Power Electronics: Handbook*", 3rd edition, Elsevier, 2011.

[Rauschenbach 1980]

H.S. Rauschenbach, "*Solar Cell Array Design Handbook*", 1st ed., Springer, 1980.

[Sanders and Kandrot 2010]

J. Sanders and Kandrot, "CUDA by Example: An Introduction to General-Purpose GPU Programming", Adisson-Wesley, Boston, USA, 2010.

[Segundo 2010]

J. Segundo, "Nonlinear Analysis of Power Systems including FACTS and Custom Power Devices based on Bifurcation Theory and Newton Methods", PhD Thesis, Division de Estudios de Posgrado, UMSNH, Morelia, Michoacán, México, 2010.

[Segundo and Medina 2008]

J. Segundo, A. Medina, "Periodic Steady-State Solution of Electric Systems Including UPFCs by Extrapolation to the Limit Cycle", *IEEE Transactions On Power Delivery*, vol. 23, no. 3, pp. 1506-1512, Jul. 2008.

[Semlyen *et al*. 1997]

A Semlyen, E Acha, and J. Arrillaga, "Harmonic Norton Equivalent for the Magnetizing Branch of a Transformer", in *Proc. Inst. Elect. Eng. C*, vol. 134, no. 2, pp. 162-169, Mar. 1997.

[Semlyen and Medina 1995]

A. Semlyen, A. M. Rios, "Computation of the Periodic Steady State in Systems with Nonlinear Components using a Hybrid Time and Frequency Domain Methodology", *IEEE Transactions on Power Systems*, vol. 10, no. 3, pp. 1498-1504, Aug. 1995.

[Smith *et al*. 1995]

B. C. Smith, A. Wood, and J. Arrillaga, "A Steady State Model of the ad-dc Converter in the Harmonic Domain", *Proc. Inst. Elect. Eng. C*, vol. 142, no. 2, pp. 109-118, Mar. 1995.

[Sokolov and Shmilovitz 2008]

M. Sokolov and D. Shmilovitz, "A Modified MPPT Scheme for Accelerated Convergence," *IEEE Trans. Energy Convers.*, vol. 23, no. 4, pp. 1105-1107, Dec 2008.

[Sood and Bhalla 2009]

V. K. Sood and P. Bhalla, "EMTP Model of a Grid-Connected PV System", Proc of the Transmission & Distribution Conference & Exposition: Asia and Pacific, pp. 1-4. 2009.

[Tan *et al*. 2004]

Y. T. Tan, D. S. Kirschen, and N. Jenkins, "A Model of PV Generation Suitable for Stability", *IEEE Trans. Energy Convers.*, vol. 19, no. 4, pp. 748-755, Dec 2004.

[Victorian Project 2017]

154 MW Victorian Project [Online]. Available: www.solarsystems.com.au

[Villalva *et al.* 2009]

M. G. Villalva, J. R. Gazoli, E. R. Filho, "Comprehensive Approach to Modelling and Simulation of Photovoltaic Arrays", *IEEE Transactions on Power Electronics*, vol. 24, no. 5, pp. 1198-1208, May 2009.

[Willis and Scott 2000]

H. L. Willis and W.G. Scott, Distributed Power Generation: Planning and Evaluation. New York: Marcel-Dekker, 2000.

[Xu *et al*. 1991]

W. Xu, J. R. Marti, and H. W. Dommel, "A synchronous machine model for three-phase harmonic analysis and EMTP initialization", *IEEE Transactions on Power Delivery*, vol. 6, no. 4, pp. 1530-1538, Nov. 1991.

[Xu *et al*. 2000]

W. Xu, H. W. Dommel, M. B. Huges, and L. Tan, "Modeling of Adjustable Speed Drives for Power Systems Harmonic Analysis", *IEEE Transactions on Power Sys*, vol. 14, no. 2, pp. 595-601, Apr. 2000.

[Xu *et al.* 1999]

W. Xu, J. R. Marti, and H. W. Dommel, "Harmonic Analysis of Systems with Static Compensators", *IEEE Transactions on Power Delivery*, vol. 6, no. 1, pp. 183-190, Feb. 1999.

[Yazdani *et al.* 2011]

A. Yazdani, A. R. Di Fazio, H. Ghoddami, M. Russo, M. Kazerani, J. Jatskevich, K. Strunz, S. Leva, J. A. Martinez, "Modeling Guidelines and a Benchmark for Power System Simulation Studies of Three-Phase Single-Stage Photovoltaic Systems", *IEEE Transactions on Power Electronics*, vol. 26, no. 2, pp. 1247-1264, April 2011.